

Universität Münster

BACHELOR THESIS

Measurement of the optical properties of PMT components and investigation of their influence on the simulated PMT response

Supervisor: Prof. Dr. Alexander Kappes

Second examiner:
Dr. Volker Michael Hannen

A thesis submitted in fulfilment of the requirements for the degree of

Bachelor of Science at Universität Münster

by

Timon Lukas Brand

AG Kappes Institut für Kernphysik

Münster, September 2025

Contents

1	Intr	oduction	1						
2	Neutrino Astronomy								
_	2.1	·							
	2.2	Cherenkov Radiation	2 3						
	2.3	IceCube Neutrino Observatory	4						
	2.3		5						
	2.4	Photomultiplier Tubes	6						
		r · · · · · · · · · · · · · · · · · · ·							
		2.4.2 Performance Parameters	7						
3	Inte	grating Sphere	9						
	3.1	General Theory of an Integrating Sphere	9						
	3.2	Transmission and Reflection Measurements	10						
4	Maa	announced of autical Duamenties of DMT Common auto	12						
4		surement of optical Properties of PMT Components							
	4.1	Experimental Setup and Software	12						
	4.2	Calibration	13						
	4.3	Transmission Measurements	16						
		4.3.1 Bandpass Filters	16						
		4.3.2 PMT Glass	19						
	4.4	Reflection Measurements of PMT Components	20						
5	Simulation of the PMT Response 24								
	5.1	Geant4	24						
	5.2	Simulating PMT Sensitivity with OMSim	24						
		5.2.1 PMT Matching	25						
		5.2.2 Effective Area Scans	28						
		Single PMT	29						
		mDOM	31						
		mbom	31						
6	Sum	amary and Outlook	33						
A	App	endix	35						
Bi	bliog	raphy	39						
Ac	knov	vledgements	42						
De	clara	tion of Academic Integrity	43						

1 Introduction

For thousands of years, humans have looked up at the night sky, wondering what unimaginable things lie beyond. This enduring curiosity has inspired countless inventions and scientific progress, allowing us to learn more and more about the universe. First, telescopes transcended the number of objects observable by the human eye. Today we are in a multi-messenger era of astronomy, where detectors specialize for one kind of messenger, like radiation or high-energy protons as part of cosmic rays, and combine their detected events to get a grasp of the universe. One of the most promising methods for observing high-energy phenomena at cosmological distances is neutrino astronomy. Unlike other astronomical messengers, the nature of neutrinos allows them to be traced directly back to their production site. These weakly interacting particles have such a low interaction cross section that they arrive undisturbed upon detection [1]. Thus, detection itself is challenging, for which largescale detector volumes are required. The largest among them to date is the IceCube Neutrino Observatory, located at the South Pole. Within a volume of about one cubic kilometer, 86 vertical strings reach depths of 2450 m in Antarctic ice, instrumenting digital optical modules (DOMs) housing photomultiplier tubes (PMTs) [2]. These aim to detect Cherenkov light that is emitted by highly energetic charged secondary leptons, produced by neutrinos interacting with ice.

Since its full commissioning in 2011, IceCube has detected around 30 neutrinos per year with astrophysical origin [3], among them the first two extragalactic neutrinos in the PeV energy range in 2013 [4]. In addition to several contributions to cosmic ray physics, the search for dark matter and multi-messenger astrophysics overall, these successes laid the foundation for two extensions of IceCube, namely IceCube Upgrade and IceCube-Gen2, with the goal of enhancing sensitivity and energy range [3, 5]. With IceCube Upgrade, new optical modules will be deployed, including the multi-PMT Digital Optical Module (mDOM), which incorporates 24 photomultiplier tubes into a single optical module. For data analysis, it is of key interest to understand the characteristics of these photomultipliers.

This thesis focuses on characterizing optical properties of internal PMT components and evaluating their impact on a simulated PMT efficiency. Subsequent to an introduction to neutrino astronomy, the results of reflectance measurements of internal PMT components are shown and compared to measurements made in [6]. These results are then introduced into a simulation of the PMT model, investigating their influence on the PMT's sensitivity.

2 Neutrino Astronomy

In the 1930s, basic physical laws seemed to be broken as conservation of energy and angular momentum was not given for beta decays of atomic nuclei. This led Wolfgang Pauli to the postulation of another particle to participate in these decays, today known as the neutrino [7]. This chapter provides a brief overview of the fundamental properties of neutrinos, their interaction with matter and detection principles. Lastly, an introduction to the IceCube Neutrino Observatory and photomultiplier tubes is given.

2.1 Neutrino Properties

Neutrinos are elementary particles in the Standard Model of particle physics. This model comprises two types of elementary particles, quarks and leptons, as the basic building blocks for known matter. Having no electric charge and being part of the lepton family, neutrinos interact only through the weak force. Interactions via gravitational force are negligible because neutrinos are nearly massless. Until now, only upper limits for their mass have been determined, the latest of them being $m_{\nu} < 0.45 \, \mathrm{eV}$ resulting from measurements with the KATRIN¹ experiment [8]. The weak interaction is carried out through exchange particles, namely the W^+ -, W^- - and Z^0 -bosons [7]. There are three different neutrino-flavors, the electron neutrino ν_e , the muon neutrino ν_μ and the tau neutrino ν_τ , each of them being the counterpart to the accordingly named other three leptons. Several studies have shown that neutrinos oscillate between these three flavors with the consequence that neutrinos have a non-zero mass, contradictory to the Standard Model in which neutrinos are considered to be massless [7].

Neutrinos originate from several sources. Atmospheric neutrinos are produced when primary cosmic rays interact with nitrogen and oxygen in the atmosphere. Among the products of these interactions are charged pions, which decay into a muon and a muon neutrino. Subsequently, the decay of muons produces electron neutrinos. Another source is the Sun. Alongside the nuclear fusion of its hydrogen to helium, solar neutrinos are produced. Of most interest to neutrino astronomy are (extra-)galactic neutrinos originating from the most extreme events in the cosmos. For example, during the process of a supernova explosion, a high intensity *neutrino burst* is produced when electrons are forced into protons, thereby creating a neutron star. Binaries consisting of a pulsar and a star rotating around their common center of mass are assumed to accelerate particles to immense energies, resulting in highly energetic neutrinos in subsequent decays. Neutrinos are able to escape these extreme events and, if detected, point back to these sources [1].

.

¹KArlsruhe TRItium Neutrino Experiment.

Because of the properties of neutrinos explained above, it is only possible to detect them indirectly via charged secondary particles produced by interactions between matter and neutrinos. Two cases are distinguished, referring to the exchanged boson. The neutral current (NC) represents interactions with the exchange of a Z^0 -boson, the term charged current (CC) is used for interactions with the W^\pm -bosons [7]. For neutrino energies above $10\,\mathrm{GeV}$, interactions are dominated by deep inelastic scattering [9] and the reactions can be written as follows:

$$v_l + N \xrightarrow{Z^0} v_l + X, \qquad v_l + N \xrightarrow{W^{\pm}} l + X,$$

where v_l denotes a neutrino with the lepton flavor l, N is a nucleon and X represents one or more hadronic particles as products of the interaction. The hadrons and leptons produced through these interactions make the indirect detection of neutrinos possible, as they can emit Cherenkov radiation inside the detector volume.

2.2 Cherenkov Radiation

Passing through a medium with refractive index n, a charged particle induces temporary dipoles along its track. These dipoles radiate electromagnetic waves. If the particle velocity remains below the speed of light in the medium $c_n = c_0/n$, these waves interfere destructively. However, once it exceeds the speed of light in the medium, constructive interference occurs, emitting electromagnetic radiation, known as Cherenkov radiation [11]. Cherenkov radiation is emitted in the form of a cone with an opening angle θ_c as shown in the illustration fig. 2.2.1. With this sketch, one can deduce the equation for the opening angle:

$$\cos \theta_c = \frac{c_0 \cdot t \cdot n^{-1}}{\beta \cdot c_0 \cdot t} = \frac{1}{\beta \cdot n},$$

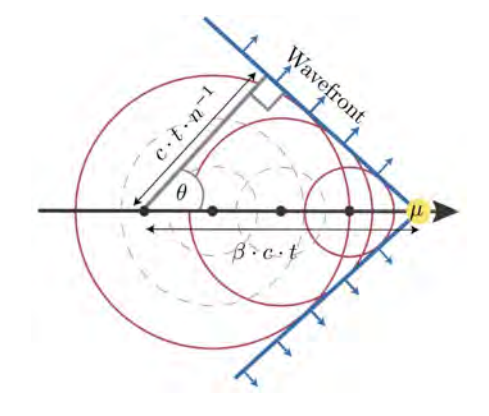


FIGURE 2.2.1: Schematic of Cherenkov radiation. In this case a muon passes through a medium at a velocity of $\beta \cdot c_0$. Taken from [10].

with $\beta = v/c_0$ being the ratio of the speed of the particle v to the speed of light c_0 .

In order to use the Cherenkov effect, a transparent and dielectric medium is needed. Additionally, because of the complexity of detecting neutrinos with such small interaction cross sections, the medium has to be of immense volume. Therefore, water or ice are primary candidates for Cherenkov detection [1]. The photons can then be detected via photomultiplier tubes (PMTs), as is done with the IceCube Neutrino Observatory.

2.3 IceCube Neutrino Observatory

The IceCube Neutrino Observatory is a cubic-kilometer Cherenkov detector located at the Amundsen-Scott South Pole Station. It consists of an array of Digital Optical Modules (DOMs) deployed in the ice beneath the surface, including a more densely instrumented sub-array DeepCore and the IceTop surface array [2]. An illustration is shown in fig. 2.3.1.

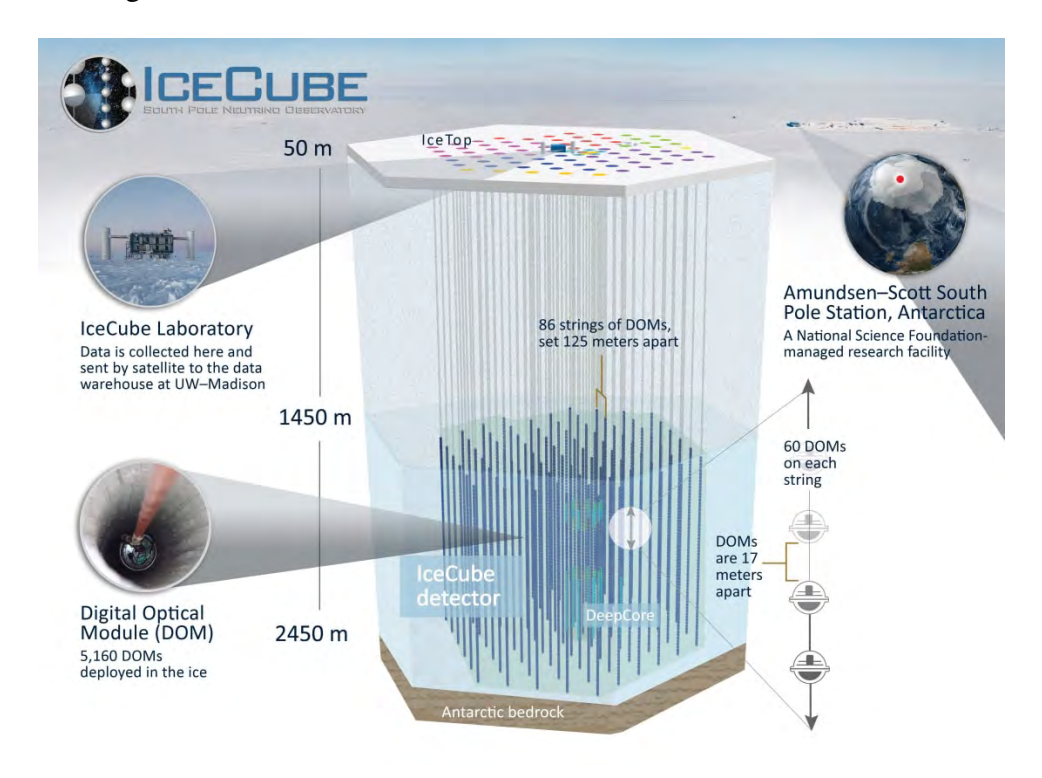


FIGURE 2.3.1: Illustration of the IceCube Neutrino Observatory. Taken from [12].

In the detector area, 86 vertical strings reach down into the ice, with 5160 DOMs deployed between depths of $1450\,\mathrm{m}$ and $2450\,\mathrm{m}$. The vertical spacing of $17\,\mathrm{m}$ between the DOMs and the horizontal spacing of $125\,\mathrm{m}$ between the strings allow the detection of astrophysical neutrinos in the energy range of $\mathcal{O}(\text{TeV})$ - $\mathcal{O}(\text{PeV})$, with $100\,\mathrm{GeV}$ being the lower energy threshold for most analyses. The DeepCore subarray consists of eight more compactly deployed strings in addition to seven central standard strings. The vertical spacing of the DOMs on the specialized strings is reduced to $7\,\mathrm{m}$ for $50\,\mathrm{DOMs}$ located at depths of $2100\,\mathrm{m}$ - $2450\,\mathrm{m}$. In total, DeepCore creates a denser instrumented volume, increasing efficiency and sensitivity, lowering the energy threshold to about $10\,\mathrm{GeV}$ [2]. IceTop is a cosmic ray air shower array located on the surface. 162 ice-filled tanks, equipped with two DOMs, are arranged in 81 stations on approximately the same grid as the in-ice array. They detect air showers initiated by cosmic rays and serve as a partial veto for the background of down-going atmospheric muons [13].

In the future, two major expansions are set to improve the overall capability of IceCube, as illustrated in fig. 2.3.2. IceCube Upgrade will deploy seven new strings with more than 700 devices and optical sensors in the DeepCore area, approximately 400 of which are mDOMs [3]. In these modules, 24 three-inch PMTs are arranged

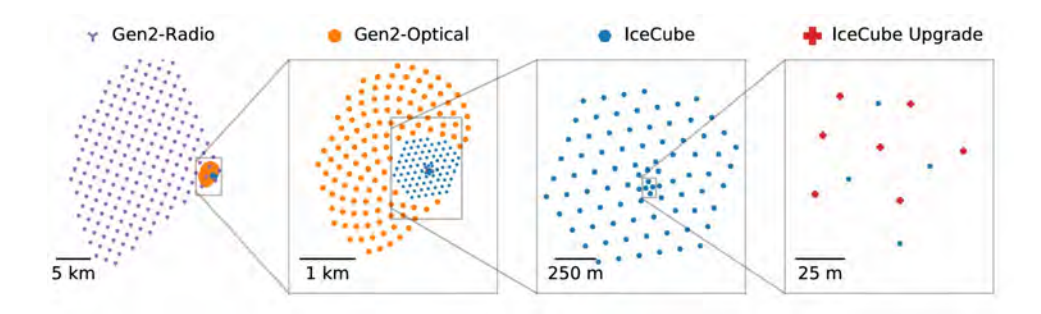


FIGURE 2.3.2: Graphical overview of IceCube Upgrade and IceCube Gen2 in top-view. Taken from [3].

within a pressure vessel uniformly in all directions, providing near-homogeneous angular acceptance, as opposed to DOMs which house a single ten-inch PMT [14].

The overall goal is to improve detection efficiency and calibration capability of the detector. More specifically, the energy threshold will be reduced to around $1\,\mathrm{GeV}$ and the capability of neutrino oscillation analyzes will increase, enabling the detection of tau neutrino appearances with high precision [5]. IceCube-Gen2 intends to increase the sensitivity by a factor of five and the number of neutrinos collected by a factor of ten. To achieve this, an extension of the optical array to $8\,\mathrm{km}^3$ and a $500\,\mathrm{km}^2$ radio array consisting of 200 stations are proposed for the detection of ultra-high-energy neutrinos (see fig. 2.3.2). In the optical high-energy array, 120 new strings spaced $240\,\mathrm{m}$ apart equipped with 80 optical modules each are to be embedded in the ice [3].

2.4 Photomultiplier Tubes

A wide range of scientific applications require photodetectors with optimal performance in optical detection. Photomultiplier tubes combine a fast response speed with high sensitivity, enabling the detection of very low light levels, down to single photons. They make use of the external photoelectric effect, where light strikes a photocathode placed in a vacuum, emitting electrons into the vacuum [15].

A PMT (see fig. 2.4.1) consists of an entrance window, a photocathode, focusing electrodes, dynodes and an anode, all sealed into an evacuated glass corpus. When a photon with sufficient energy strikes the photocathode², a photoelectron is released through the external photoelectric effect into the vacuum. The photoelectron gets accelerated towards the first dynode, which is on a higher potential. Upon its way, focusing electrodes ensure that the photoelectron strikes the first dynode. On impact, a photoelectron releases a multitude of secondary electrons³, which are accelerated to the next dynode. Through this multiplication system, the original input of a single photon is transformed into a measurable signal that can be extracted as voltage or charge by the anode at the end of the system [15].

²Made out of alkali metals. Typically, bialkali compounds (Sb-K-Cs, Sb-Rb-Cs) or multialkali compounds (Sb-Na-K-Cs) are used for photon detection in range from ultraviolet to near-infrared [15].

³Normal secondary emission ratio is 3 to 5 for an interstage voltage of 100 V but values > 10 for higher voltages are possible [15].

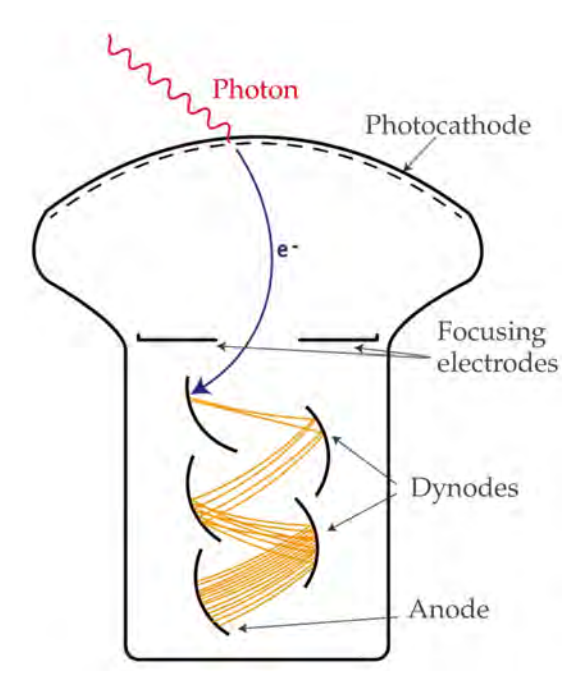


FIGURE 2.4.1: Schematic of a photomultiplier tube. A photon (red sinusoidal line) strikes the photocathode and releases an electron (blue line). Secondary electrons (yellow lines) are emitted by the dynodes. Taken from [6].

The IceCube Neutrino Observatory uses PMTs housed in transparent pressure vessels to detect Cherenkov light. For data analysis, it is essential to fully understand the characteristics of the PMTs. Therefore, simulation of optical modules and photomultiplier tubes provides valuable information on how to interpret real detection events. In this thesis, measurements of internal reflections in the photomultiplier tubes are incorporated into a simulation that includes PMTs and optical modules, enabling an estimation of their sensitivity.

2.4.1 Reflections at internal Components

The importance of the aforementioned measurements lies in the fact that photons can be transmitted through the photocathode, which are then potentially reflected, possibly releasing a photoelectron on their way back out of the PMT. A simplified sketch of these events is shown in fig. 2.4.2. On first impact (position 1), several photoelectrons are released. Photons that do not release a photoelectron can be transmitted and then reflected at the internal components (position 2) marks the inner reflective coating in this case) and subsequently cross the photocathode again (position 3) with the probability of releasing photoelectrons. Although this sketch is simplified, as

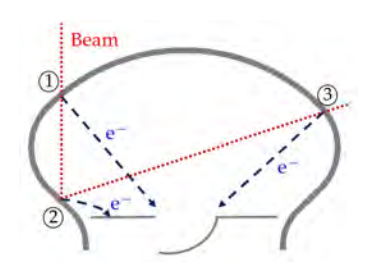


FIGURE 2.4.2: Sketch of a PMT illuminated with a collimated beam. See text for further explanation. Taken from [6].

it does not include secondary reflections from the optical boundaries [6], it highlights

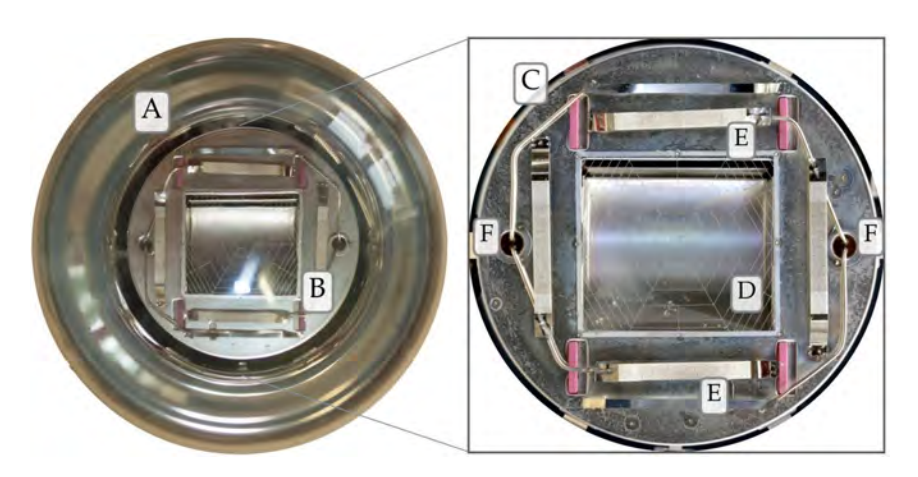


FIGURE 2.4.3: Photograph of frontal view of a PMT. See text for explanation of the labels. Taken and modified from [6].

the importance of knowing the reflectance of the internal parts for proper simulation of the photomultiplier response.

The photograph in fig. 2.4.3 shows the relevant internal components of a PMT. The inner reflective coating (A) covers the lower half of the glass bulb. The coating is the electrical conductor connecting the photocathode layer and the wire leading to the cathode, such that the voltage supplied by the PMT base can reach the photocathode [6]. In the enlarged image, the front of the electron multiplier system (B) can be seen, which holds the following internal parts: The circular front plate (C) serves as a structural base that connects all parts. The rectangular entrance to the first dynode (D) is located in the center. Thin wires in a web^4 pattern, serving as additional focusing electrodes, are visible in front of the main dynode. Together with thin rectangular plates (E), which are presumed to participate in the photocathode evaporation process [16]. Lastly, two entrance holes (F) can be identified that lead wires which connect to the rectangular plates. In this thesis, the optical properties of the main parts that contribute to reflections (inner reflective coating, circular frontal plate, first dynode and the rectangular plates) shall be investigated.

2.4.2 Performance Parameters

The wavelength-dependent **quantum efficiency** (QE) is defined as the ratio of photoelectrons emitted by the photocathode to incident photons and therefore displays the photocathode sensitivity. QE differs according to the compound of alkali metals and additional factors, but is typically in the range of 20 - 30% for bialkali photocathodes [15].

Incoming photoelectrons that strike a dynode release a multitude of secondary electrons. The ratio of outgoing to incoming electrons is referred to as secondary emission yield or **gain** δ . Without scattering losses, the relationship between interdynode voltage ν and gain may be assumed to be linear with α describing the proportionality. Accounting for electrons that undergo inelastic scattering, which reduces electron energy, leads to an exponent $\beta < 1$. Thus, the gain for one dynode follows

⁴Often referred to as a mesh or spider.

the semi-empirical equation [17]:

$$\delta = \frac{N_{\text{out}}}{N_{\text{in}}} = \alpha \cdot \nu^{\beta}.$$

The total gain G of the multiplication system with n dynodes can be expressed as the product of the individual dynode gains, which can then be rewritten with the overall voltage V between photocathode and anode, since this voltage is distributed via a voltage divider between the dynodes. This leads to the following equation [6]:

$$G = \prod_{k=1}^{n} \alpha_k \cdot \nu_k^{\beta_k} = a \cdot V^b.$$

Another parameter that is important for optimizing the performance of the PMT is the **collection efficiency** F. It is defined as the ratio of single photoelectrons that leads to a signal at the anode to the total number of photoelectrons released at the photocathode [15]. Furthermore, the **detection efficiency** DE of a PMT is defined as

$$DE(\lambda) = F \cdot QE(\lambda).$$

Depending on the read-out mode, the signal from the anode is read out as a voltage or as a charge signal. At high light intensities, the current or analogue mode is used to determine the charge by integrating the signal within a certain time window. For lower intensities, single pulses can be distinguished as opposed to the previous case. Now, the pulse- or photon-counting mode is applicable, supplying the analogue signal to a resistor. This results in a voltage drop, which is schematically shown in fig. 2.4.4. This allows the determination of several timing parameters, such as the **transit time** (TT) of the PMT which is the total time elapsed between photoelectron emission at the photocathode and the associated pulse response at the anode⁵. Since electrons can

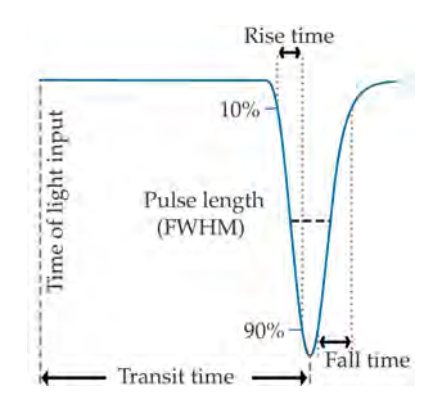


FIGURE 2.4.4: Schematic illustration of a measured PMT pulse with characteristic timing parameters. Taken from [6].

take different paths due to their point of origin on the photocathode or due to different initial conditions at the same point (energy and direction of emission), the transit time varies. This is referred to as **transit time spread** (TTS) and is estimated as standard deviation or FWHM of the transit time distribution [15].

⁵Direct measurement of the TT intrinsic to the PMT is quite challenging as usually the elapsed time in respect to the light source trigger signal is measured. One possibility is to measure the time elapsed between the trigger of a reference diode with same cables as the PMT and the signal at the anode of the PMT.

3 Integrating Sphere

An integrating sphere is a device for measuring optical radiation. It has a diffuse reflective coating (also called Lambertian surface) on the inner surface. For ideal spheres, this means that incident light is distributed uniformly over the sphere after reflection on the inner surface of the sphere [18]. In reality, the sphere has port openings for placing samples, attaching a detector device and for light input. This changes the average reflectance of the sphere and needs to be taken into account when assessing the measured radiance. In this chapter, the general theory of integrating spheres is introduced, after which methods for transmission and reflection measurements are presented.

3.1 General Theory of an Integrating Sphere

In general, the radiance L of a diffuse surface can be expressed as

$$L = \frac{\Phi_i \rho}{\pi A},$$

for an incident flux Φ_i , where ρ is the reflectance, A is the illuminated area and π is the total projected solid angle from the surface [18]. To derive the radiance for the entire sphere, multiple surface reflections and losses through port openings need to be considered. In case of a sphere with two port openings (indices i and e), the flux incident on the entire surface (index s) of the sphere after the initial reflection can be denoted as the following [18]:

$$\Phi_{s,1} = \Phi_i \rho \left(\frac{A_s - A_i - A_e}{A_s} \right).$$

The term in parentheses can be shortened and expressed as (1-f) with $f=(A_i+A_e)/A_s$ representing the fraction of the area where losses occur. The second reflection produces an amount of flux incident on the sphere surface that can be denoted as

$$\Phi_{s,2} = \Phi_i \rho^2 (1 - f)^2.$$

By similar reasoning, these equations can be expanded to n reflections. As the input flux Φ_i is continuous, all reflections are measured at the same time, so the total flux after n reflections is [18]:

$$\Phi_n = \Phi_i \rho(1-f) \left\{ 1 + \rho(1-f) + \ldots + \rho^{n-1} (1-f)^{n-1} \right\}.$$

The expression can then be expanded to an infinite power series, and as $\rho(1-f) < 1$, the geometric series converges to a compact equation [18]:

$$\Phi_{\text{tot}} = \frac{\Phi_i \rho (1 - f)}{1 - \rho (1 - f)}.$$

Ultimately, the sphere surface radiance is given by the following equation [18]:

$$L_{s} = \frac{\Phi_{i}}{\pi A_{s}(1-f)} \cdot \frac{\rho(1-f)}{1-\rho(1-f)} = \frac{\Phi_{i}}{\pi A_{s}} \cdot \underbrace{\frac{\rho}{1-\rho(1-f)}}_{M},$$
 (3.1.1)

where M is often referred to as the sphere multiplier.

However, eq. (3.1.1) was derived considering only two port openings. In reality, one will have to consider various ports that can also hold samples or devices with a reflectance different from the reflectance of the sphere wall. This leads to the general expression for the sphere multiplier [18]:

$$M = \frac{\rho_0}{1 - \rho_w \left(1 - \sum_{i=0}^n f_i\right) - \sum_{i=0}^n \rho_i f_i} = \frac{\rho_0}{1 - \overline{\rho}}.$$
 (3.1.2)

Here, ρ_0 denotes the initial reflectance for incident flux, ρ_w represents the reflectance of the sphere wall, ρ_i the reflectance of port opening i and f_i is the fractional port area of port opening i. The equation can be written in a short form with the average sphere reflectance $\overline{\rho}$.

3.2 Transmission and Reflection Measurements

To perform transmission or reflection measurements, a sample is placed at the entrance port of the integrating sphere or at the exit port, respectively. In fig. 3.2.1 the two standard cases are illustrated. Furthermore, it can be seen that a baffle is integrated into the sphere. A baffle is needed to prevent light that is directly reflected from the sample from being detected, as it would yield a false response [18]. The baffle is coated with the same diffuse reflective material as the sphere wall.

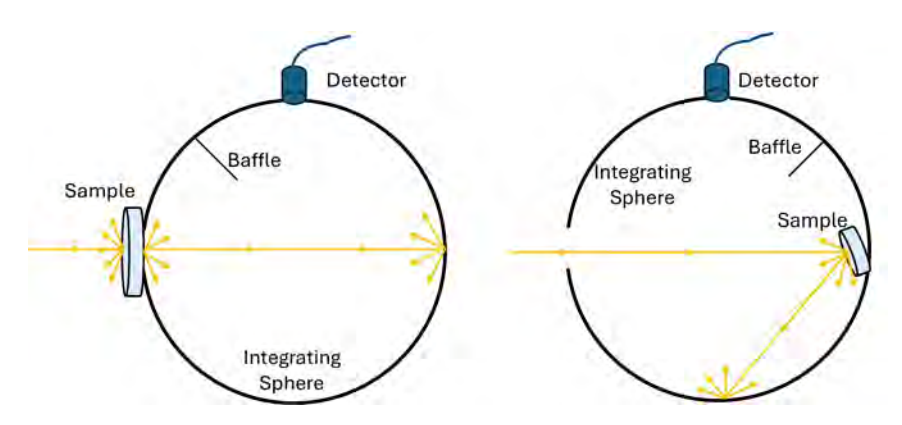


FIGURE 3.2.1: Schematic illustration of transmission (left) and reflection (right) measurements.

To assess the reflectance of a material, a reference sample with a known reflectance is needed. If the samples are simply substituted between each measurement, the average sphere reflectance in each measurement would not be the same. Utilizing eq. (3.1.1) and eq. (3.1.2) the following equation can be obtained [18]:

$$\frac{L_s}{L_r} = \frac{\rho_s}{\rho_r} \cdot \frac{1 - \overline{\rho}_r}{1 - \overline{\rho}_s},\tag{3.2.1}$$

where the index s refers to the measurement with the sample and the index r marks the reference measurement. However, $\overline{\rho_s}$ depends on ρ_s , hindering the general determination of ρ_s .

This problem can be avoided by using the comparison method. If both the sample and the reference are mounted simultaneously on two different ports as shown in fig. 3.2.2, the average sphere reflectance can be kept constant. In contrast to what fig. 3.2.2 might suggest, the samples are not illuminated at the same time. If the entrance port remains the same, the two samples can be simply switched between the measurements. Now that the average sphere reflectance is the same, eq. (3.2.1) reduces to

$$\frac{L_s}{L_r} = \frac{\rho_s}{\rho_r} \tag{3.2.2}$$

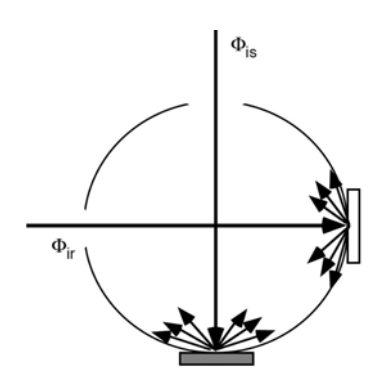


FIGURE 3.2.2: Schematic principle of the comparison method. Taken from [18].

allowing the determination of ρ_s because L_s and L_r are measured and ρ_r is known [18]. The comparison

method can also be applied to transmission measurements. In this case, the reference measurement is performed with an open port, which means that the sample can simply be switched between two open ports and eq. (3.2.2) can be used with $\rho_r = 1$.

4 Measurement of optical Properties of PMT Components

In this chapter, the results of several measurements, performed with an experimental setup containing an integrating sphere (see chapter 3), are presented. Firstly, the experimental setup is introduced, followed by the calibration of the spectrometer. The first measurements shown examine the transmission of bandpass filters and the absorption length of a PMT's glass bulb. Finally, the main reflection measurements on the internal PMT components (first introduced in section 2.4) are presented and compared to similar measurements made in [6].

4.1 Experimental Setup and Software

In fig. 4.1.1 the general experimental setup is shown. All measurements use a xenon lamp⁶, an integrating sphere⁷, an optical fiber⁸ and a spectrometer⁹ equipped with a CCD (Charged Coupled Device) camera¹⁰. Various custom 3D-printed brackets are used to mount samples at different ports. The diffuse reflective coating of the integrating sphere is made of Spectralon (PTFE) offering more than 99 % reflectance

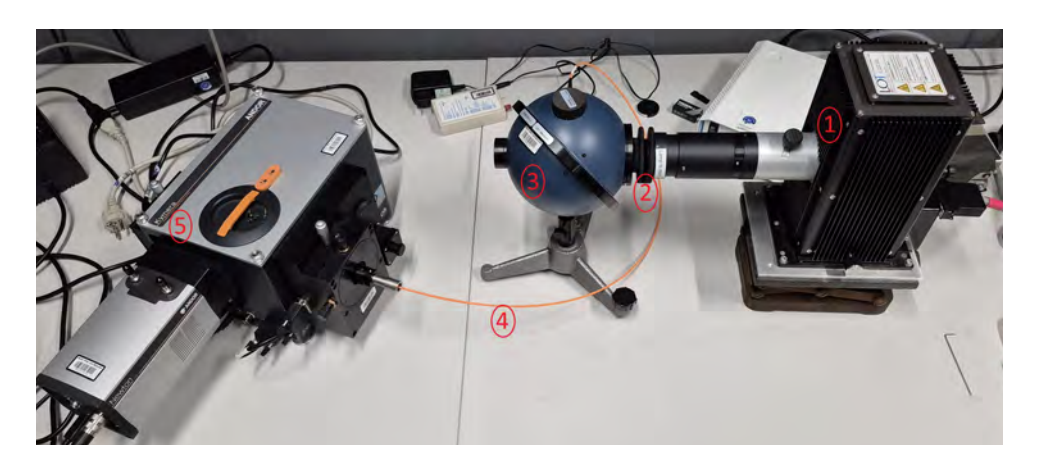


FIGURE 4.1.1: Picture of the general setup showing the xenon lamp (1), a bracket for a sample (2), the integrating sphere (3), an optical fiber (4) and the spectrometer (5). The setup undergoes slight modifications for the different measurements.

⁶LOT LSE140 / 160.25.C.

⁷Newport 819C-IS-5.3 [19].

⁸Thorlabs M114L01 [20].

⁹Andor Solis Kymera 193i-B1 [21].

¹⁰Andor Solis Newton CCD DU920P-OE [22].

from $400\,\mathrm{nm}$ - $1500\,\mathrm{nm}$ and more than $95\,\%$ from $250\,\mathrm{nm}$ - $2500\,\mathrm{nm}$ [19]. The signal from the CCD sensor can be obtained by software¹¹.

The light collected by the optical fiber is directed through the spectrometer. There it is vertically dispersed into its spectral components which then illuminate the CCD-sensor with its 1024x255 pixels [22]. In theory, each of the 255 vertical pixel lines now corresponds to one specific wavelength. The pixels are individual photosensors that produce photoelectrons when exposed to light. In this way, electrons are collected in every pixel and a charge pattern is accumulated. This charge pattern is extracted and digitalized by shifting the charge pattern stepwise into the so-called shift register and subsequently into an output node of an amplifier that is fed to an analog-to-digital converter [23]. In this process, the whole charge pattern is maintained. In measurements with the spectrometer, every column of the sensor corresponds to a specific wavelength. Consequently, it is sufficient to read the charge stored in whole columns, which is done by full vertical binning (FVB). Unless otherwise specified, all measurements presented in the following are taken with FVB, which can be selected in the acquisition setup of the software.

Further preparations and settings are adjusted before each measurement. By cooling down the CCD the dark signal can be reduced [23]. Before each measurement, the sensor was cooled to a steady operation temperature of $-80\,^{\circ}$ C. In addition, the xenon lamp is switched on at least three hours before each measurement, since its intensity fluctuates during the initial warm-up period. The acquisition setup allows different acquisition modes with adjustable exposure time. The most basic of them being **Single** and **Accumulate**. A single scan reads out the CCD one time after the preset exposure time. An accumulate scan performs a number of single scans, which are summed up. With the **Wavelength Drive**, the desired wavelength range can be selected, as the width of the sensor limits the wavelengths measurable simultaneously to roughly $320\,\mathrm{nm}$. Two **gratings** (G1 with a groove density of $400\,\mathrm{L\,mm^{-1}}$ and a blaze of $250\,\mathrm{nm}$ and G2 with $399\,\mathrm{L\,mm^{-1}}$, $550\,\mathrm{nm}$) can be selected that are optimized for different wavelength ranges.

The spectrometer comes with a pre-defined calibration that converts the pixel number of the columns to wavelengths. In [6], this default calibration was used with reflection measurements. To verify reliability, the measurements are repeated with a manual calibration.

4.2 Calibration

The software offers the possibility to perform and apply a manual x-calibration. However, it only allows for a specific pixel-to-wavelength calibration, which means that the calibration is limited to one exact wavelength range. This is very impractical, which gives the reason to perform a manual wavelength-to-wavelength calibration by measuring a Mercury-Argon-Lamp with known spectral lines. This approach allows for applying the calibration to data post-measurement, regardless of the exact wavelength range.

¹¹Andor Solis Version 4.31.30023.0 [23].

The calibration lamp is shown in fig. 4.2.1. The characteristic spectral lines are given with their wavelength and relative intensity. It is possible to connect an optical fiber directly to the lamp (see the red seal in fig. 4.2.1).

For calibration, three different measurements are taken with the following wavelength ranges: 220 nm - 542 nm (G1), 500 nm - 815 nm and 650 nm - 961 nm (both G2). Due to direct coupling, an exposure time of 0.5 s in single scan mode yields a sufficient intensity. For each of the wavelength ranges, the background is measured with the same exposure time and subtracted from the respective measurement to rule out electrical noise from the sensor. This is done by closing the shutter between the light input and the inner components of the spectrometer with the software. These first measurements were not yet measured in FVB, but in a full-resolution 2D raw image. To manually convert the image to an intensity spectrum in two dimensions, the mean¹² of the pixels in one respective column is taken. Then a number of the most noticeable peaks are fitted with a Gaussian of the form



FIGURE 4.2.1: Photograph of the calibration lamp.

$$g(x) = A \cdot \exp\left(-\frac{(x - \overline{x})^2}{2\sigma^2}\right)$$

to approximate the wavelength \overline{x} and its uncertainty σ . The measured wavelengths are then plotted against their target wavelengths given on the lamp and a linear calibration is applied. Examples for both steps are shown in fig. 4.2.2.

The peak on the left is not symmetric as it shows a right *shoulder*. This can be reasoned for by the intensity map of the spectral lines showing that the spectral lines are slightly bent right towards the top and bottom of the sensor. Presumably, this is an

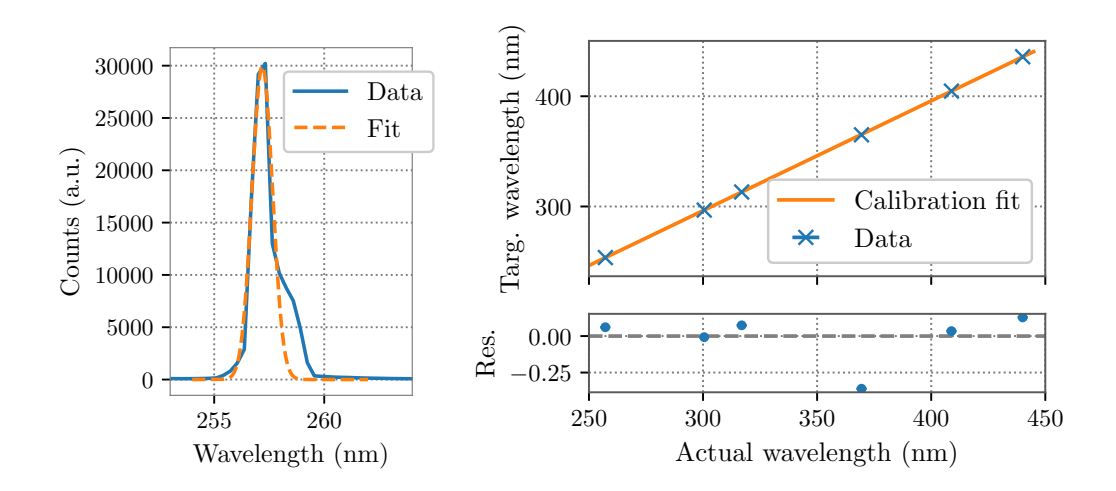


FIGURE 4.2.2: Left: Exemplary Gaussian fit. Right: Calibration fit based on the values of the Gaussian fits.

¹²In following measurements, when FVB is performed by the software, the pixels of columns are summed up, not averaged.

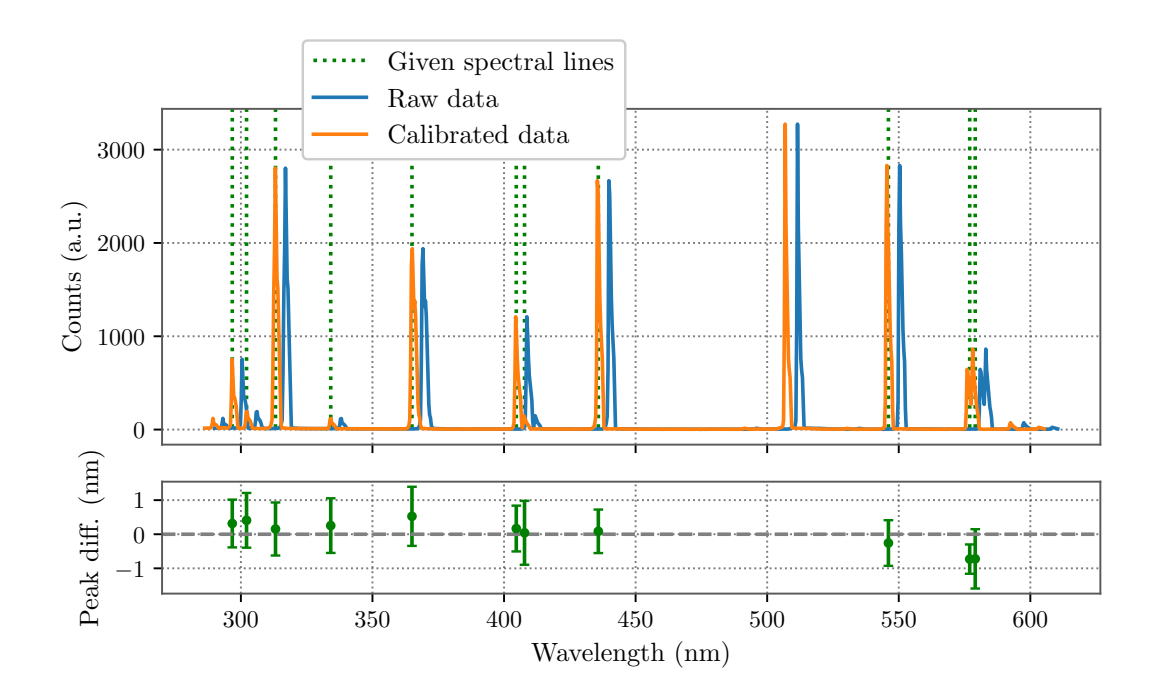


FIGURE 4.2.3: Measurements of the calibration lamp without (blue) and with (orange) calibration. The given spectral lines are indicated by the dotted lines. The sub-plot shows the difference between the calibrated peaks and their associated spectral lines.

artifact from mirror reflections inside the spectrometer as the light is guided towards the sensor. This asymmetry leads to the Gaussian fit seemingly not matching the data perfectly. However, this does not pose a problem as the peak position is accurately estimated and the effect of this right shoulder is negligible.

In fig. 4.2.3 an exemplary data acquisition is shown before and after calibration. The adjustments are small, but noticeable. A dominant peak at $\lambda \approx 509\,\mathrm{nm}$ is not marked with a corresponding spectral line because it is a second-order maximum of the $235.652\,\mathrm{nm}$ peak. These second-order peaks were already neglected for calibration. To quantify the impact of calibration, a wavelength of $\lambda = 250\,\mathrm{nm}$ is shifted by $(-3.56\pm0.49)\,\mathrm{nm}$, $\lambda = 700\,\mathrm{nm}$ undergoes a shift of $(-6.50\pm0.48)\,\mathrm{nm}$. The data points shown in the sub-plot of fig. 4.2.3 denote the difference between the calibrated peaks and their associated spectral line. It can be seen that the calibration allows an accuracy of $< 1\,\mathrm{nm}$. The possibilities of performing a quadratic or cubic calibration were also considered, but testing the different fit functions on other data sets did not yield noticeable improvements. In fact, the linear fits suited best and are from now on applied to every new data acquisition. For measurements taken with grating G1, the following fit function is used:

$$cal_{G1}(\lambda) = (0.9957 \pm 0.0011) \cdot \lambda + (-2.49 \pm 0.40) \text{ nm}.$$

For measurements with grating G2, this function based on the data set with the lower boundary 500 nm is applied:

$$cal_{G2}(\lambda) = (0.99702 \pm 0.00049) \cdot \lambda + (-4.41 \pm 0.33) \text{ nm}.$$

In the scope of this thesis, all measurements with G2 are taken in the range of around

 $500 \,\mathrm{nm}$ - $800 \,\mathrm{nm}$, which is why the data set from $650 \,\mathrm{nm}$ - $961 \,\mathrm{nm}$ is neglected for these calibration functions. If future measurements are taken in the (near) infrared region, these data may be included for calibration.

4.3 Transmission Measurements

To test the setup, some transmission measurements are carried out. The setup used for the measurements is the one shown in fig. 4.1.1. The 3D-printed bracket allows for placing the samples between the sphere and the xenon lamp by directly connecting the entrance port to the tube of the lamp. One pinhole is built into the tube to restrict the area of the collimated incident light so that only the sample is hit. Because of the direct connection between the sphere and collimation tube, it is nearly impossible for external light to enter the sphere. As the measurements are carried out in a darkened room, with only low-intensity red lamps and the computer display as light sources, interference from external light can be excluded, which was also verified.

The measurements are performed in accumulate mode with three repetitions, each using an exposure time of $10\,\mathrm{s}$. To determine the transmission of a sample, three measurements are needed: A reference measurement L_r (1) is performed without a sample to represent $100\,\%$ transmission, as light enters the sphere unimpeded. A transmission measurement L_s (2) is measured with a sample in place. The background L_b (3) is measured with the shutter closed (as explained, the background of external light sources can be neglected, so electrical noise dominates the background) and subtracted by the two other measurements. The transmittance is calculated as:

$$T(\lambda) = \frac{L_s(\lambda) - L_b(\lambda)}{L_r(\lambda) - L_b(\lambda)}.$$
(4.3.1)

4.3.1 Bandpass Filters

First, five bandpass filters ¹³ were measured. All filters are specified with $(10\pm2)\,\mathrm{nm}$ FWHM and labeled with their corresponding center wavelength. In the following, the filters are referred to as F405 if their center wavelength is $405\,\mathrm{nm}$. It should be mentioned that these measurements were not yet taken with the comparison method. Although the correction in transmittance is expected to be small, as the intensity loss in both reference and transmission measurement should be comparable for the bandpass region, this should be kept in mind for evaluation of the following results.

In fig. 4.3.1 the results for the filter F405 are shown. The specifications given by the manufacturer state over $85\,\%$ transmittance and a FWHM of $(10\pm2)\,\mathrm{nm}$ around the center wavelength $405\,\mathrm{nm}$. The results show a transmittance that this value with an average transmittance of $(91.3\pm2.5)\,\%$. To verify the FWHM, the wavelengths corresponding to $40\,\%$ and $50\,\%$ transmittance were averaged at the lower and upper ends, respectively. The subtraction yields $(10.24\pm0.16)\,\mathrm{nm}$ which aligns with the specification given by the manufacturer. It can be observed that the measured peak becomes slightly narrower at high transmittance and broader towards low transmittance. In theory, a rectangular distribution with the specified width would be ideal. In practice, imperfections in manufacturing and measurement lead to the observed peak

¹³LC-HBP series, manufactured by LASER COMPONENTS Germany GmbH.

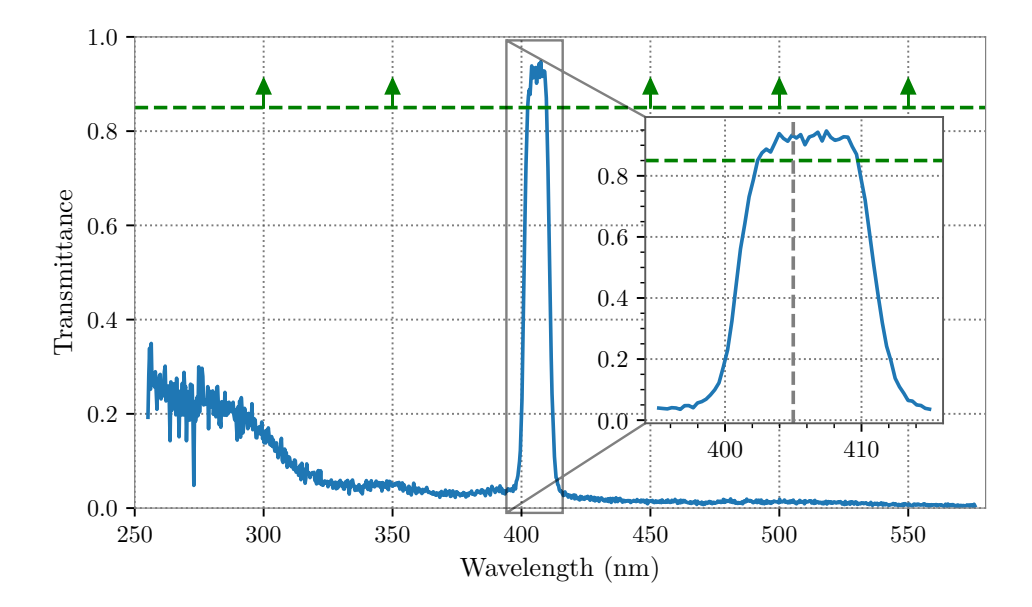


FIGURE 4.3.1: Transmittance of bandpass filter F405. The horizontal green line with its arrows indicates the transmittance specified by the manufacturer.

structure and the need to strongly suppress unwanted wavelengths reduces the width at high transmittance, while maximizing transmittance leads to a broader width at low transmittance.

Furthermore, the position of the band has to be discussed. In the results, a slight shift of $(0.935 \pm 0.079)\,\mathrm{nm}$ to higher wavelengths is observed, estimated with the wavelengths used before in the calculation of the FWHM. Nevertheless, the specification of the center wavelength $(405\,\mathrm{nm})$ is not questioned because this effect can primarily be attributed to calibration that is limited to a certain accuracy. In comparison, when calibration was checked (see fig. 4.2.3), a calibrated peak at $\lambda = (404.82 \pm 0.67)\,\mathrm{nm}$ had an accuracy of $(0.17 \pm 0.67)\,\mathrm{nm}$. Eventually, it can even be seen as a confirmation of the calibration as it averted even higher deviation.

Apart from the wavelengths in immediate proximity to the bandpass, wavelengths $>420~\mathrm{nm}$ are suppressed to an average transmittance of $(1.20\pm0.44)~\%$. The manufacturer specifies OD4 average blocking in this wavelength range, which corresponds to $T\leq0.01~\%$. The measurement results do not reflect this specification, missing it by two orders of magnitude and showing even higher transmittance at lower wavelengths. The most likely explanation is that the setup is not suitable for measuring this precision. The background removal and the exposure time of $10~\mathrm{s}$ is probably not sufficient to evaluate such a low transmittance properly. Additionally, the transmittance increases even more for low wavelengths because in this region, the xenon lamp provides a much lower intensity, worsening the signal-to-noise ratio. Furthermore, the wavelength range specified for the optical fiber is $180~\mathrm{nm}$ - $1200~\mathrm{nm}$ [20] and for the integrating sphere it is $250~\mathrm{nm}$ - $2500~\mathrm{nm}$ [19], which means that both tools operate close to the lower end of their wavelength range. In summary, the setup has limitations in this UV region. Therefore, the blocking quality of the filter is not challenged.

All filters come with an arrow on their circular frame, indicating the intended direction for the light to travel. In all results, the filters were placed with the arrow

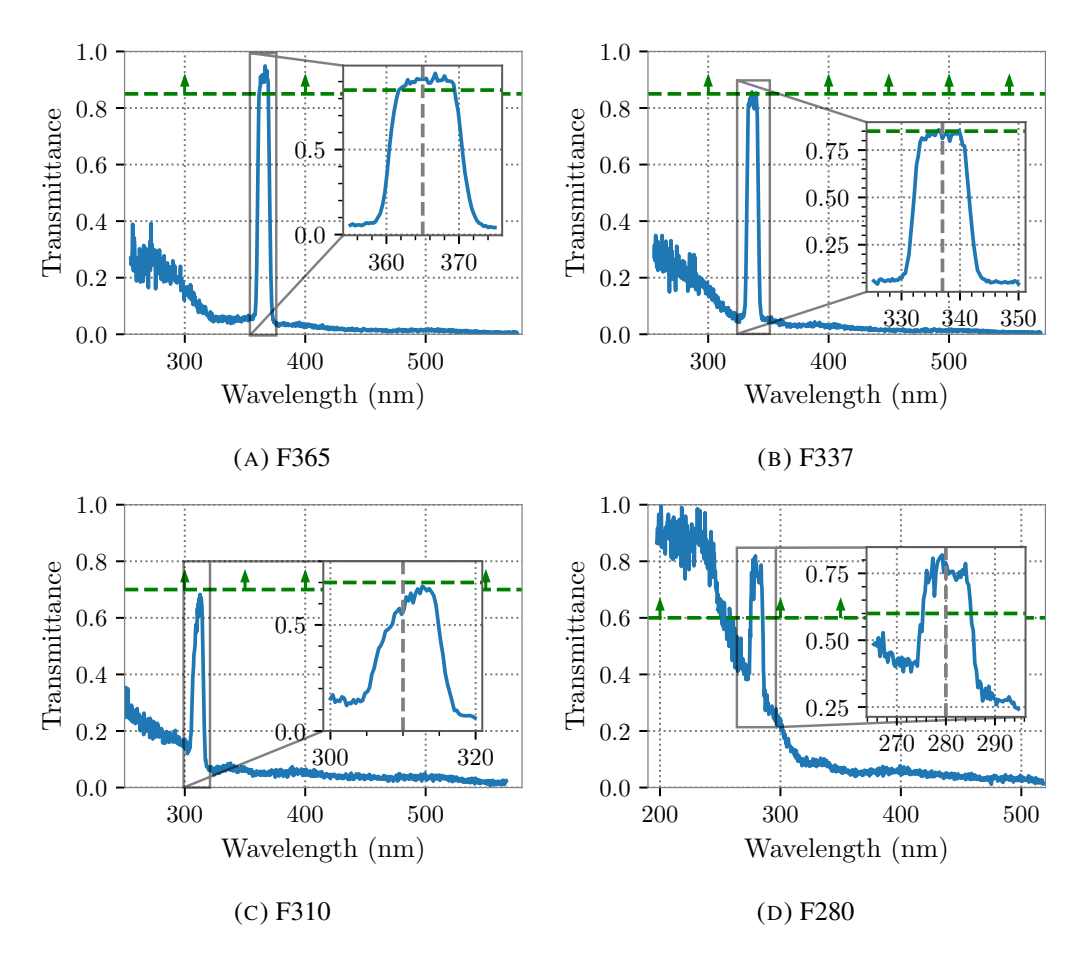


FIGURE 4.3.2: Transmittance results for other filters.

pointing in the stated direction. However, a test was performed with the arrow facing the lamp, but this yielded no noticeable difference.

In fig. 4.3.2, the results of the other four filters are shown. For F365 (measured with G2), similar results as for F405 are observable. The given specification of T > 85% is surpassed and the band width $(10 \pm 2)\,\mathrm{nm}$ is validated. The calibration seems to work even better in this wavelength range as the peak is nearly symmetrical centered around $365\,\mathrm{nm}$. The same applies for F337 (measured with G2) calibrationwise. Transmittance-wise however, the transmission averages $(82.3 \pm 2.2)\%$ at the peak, not reaching the specified T > 85%.

Filter F310 has to be investigated more closely. Unlike any other filter, this one shows an imbalance towards its lower and higher end of its band width. Furthermore, even the highest measured transmittance does not reach the given specification of > 70%. The assumption was made that the filter was placed on a certain angle so that the beam did not pass fully perpendicular to the filter. However, following the unusual results, the measurements were repeated a few times with close attention to a perpendicular beam path. Another suggestion was impurities on the filter that limit transmittance. However, the filters were always handled with gloves and dust particles were cleaned with lens cleaning tissues, so this is likely to be excluded as well. In the additional measurements, both gratings were tested (shown are the results with G1). The gratings noticeably increase measurable intensities in the region of their grating blaze. However, as this is valid for both the reference and the

filter measurements, no changes in transmittance were observed between both gratings. This leaves the supposition that this filter might not meet specifications. Filter F280 was measured with grating G1 and a lower wavelength limit of $200\,\mathrm{nm}$. As mentioned before, the general setup is not suitable for this UV region, especially $\lambda < 250\,\mathrm{nm}$ (limitation of the integrating sphere [19]). Hence, the region where transmittance appears to approach $100\,\%$ can be disregarded. The given specification of $60\,\%$ is exceeded with an average transmittance of $(77.8 \pm 2.3)\,\%$. However, for the center wavelength $280\,\mathrm{nm}$ the unwanted increase in transmittance is already present, leading to the assumption that the real transmittance is lower.

In general, it has to be said that the setup is not suitable to verify how well the out-of-band wavelengths are suppressed by the bandpasses. This especially applies to the filters F280 and F310 in UV region. If special attention is paid to suppressing the other wavelengths, these filters should be tested with a light source that grants higher intensity in this wavelength region or use distinctly higher exposure times, reducing the signal-to-noise ratio. In general, a setup more suitable for lower UV-light would be necessary.

4.3.2 PMT Glass

Since the PMT is cut open to extract the internal components, the opportunity to measure the transmittance of the PMT glass is given. Here, the comparison method, introduced in section 3.2, is used. Each of the three configurations is measured two times with G1 and G2 to cover the wavelength range 250 nm - 737 nm. The measurements were carried out in accumulate mode with three repetitions and 10 s exposure Transmittance can then be calculated via eq. (4.3.1). The results are smoothed with a Savitzky-Golay-Filter and extrapolated to zero for small wavelengths. Then, they can be converted into the absorption length via [25]:

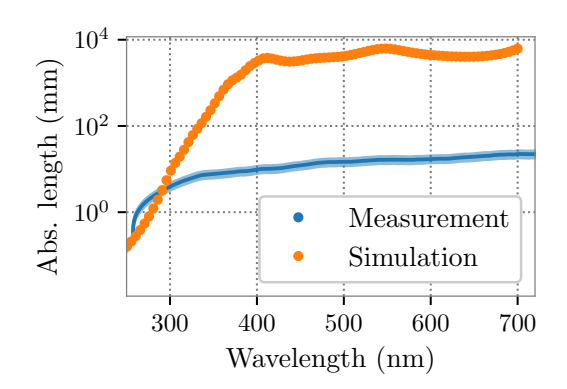


FIGURE 4.3.3: Comparison of the measured absorption length of the PMT glass with the values set in simulation (see [24]).

$$a(\lambda) = (-d)/\ln T(\lambda) \tag{4.3.2}$$

where d denotes the thickness of the glass and $T(\lambda)$ is its transmittance. For the results shown in fig. 4.3.3, $d=(2.04\pm0.40)\,\mathrm{mm}$ was used. The uncertainty was estimated because it was not possible to measure the thickness in the middle of the glass bulb and even at the edges, the thickness fluctuated. The calculated absorption length shows huge differences to the current values set in simulation (the simulation is introduced in chapter 5). The values in the simulation are based on transmittance values of the mDOM pressure vessel, which consists of borosilicate glass as the PMT. The transmittance can be calculated via eq. (4.3.2) with the thickness of the pressure vessel $d=12.5\,\mathrm{mm}$ to $99.71\,\%$ (at $\lambda=503\,\mathrm{nm}$), explaining the difference of more

than two orders of magnitude, as the transmittance measured here is only $87.09\,\%$ for this wavelength. Since the glass bulb in these measurements was only placed provisionally and was not cleaned extensively beforehand, the current simulation values are not challenged. However, measuring pressure vessel glass and PMT glass with the same preparation and setup could provide validation of the simulation values.

4.4 Reflection Measurements of PMT Components

After familiarization with the setup by completing these transmission measurements, it is finally time to measure the reflectance of the PMT components (mentioned in section 2.4). The results presented in this section are later introduced into the simulation. To extract samples from the internal parts, the glass bulb of a Hamamatsu R12199¹⁴ PMT was cut open right between the inner coating and the photocathodelayer. Thereafter, several samples of the different components are cut out, shown in fig. 4.4.1.

The measurement setup is quite similar to the one shown in fig. 4.1.1, only that the sample is now placed at the port on the opposite side of the light input. In addition, the reference is placed on the top port and vice versa. Again, for mounting the samples to a port, 3D-printed brackets are used. In order to utilize the comparison method presented in section 3.2, two brackets are needed to mount the sample and the reference at the same time. Both brackets have a square cutout (slightly smaller than the samples shown in fig. 4.4.1), behind which the sample and the reference mirror¹⁵ can be placed, respectively. This ensures an illuminated area of the same size when switching the samples, satisfying the condition made in section 3.2 that the average reflectance of the sphere must be the same. For the thin rectangular plates, two separate brackets with a cutout of their shape are

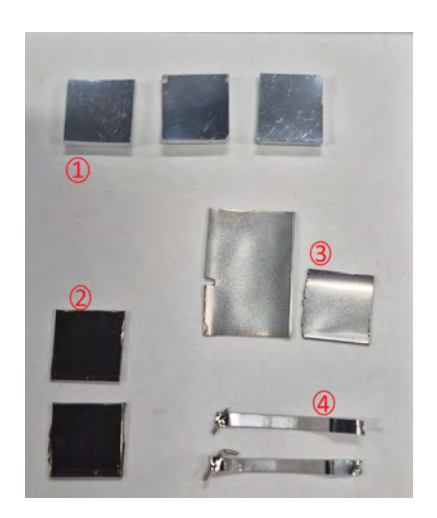


FIGURE 4.4.1: Photograph of the samples that were cut out. (1) inner coating, (2) front plate, (3) dynode, (4) rectangular flaps.

3D-printed. Furthermore, the samples and the mirror are mounted at an angle of 8° such that the specular reflected light does not immediately leave the sphere through its entrance port. The light is always reflected away from the optical fiber to avoid measuring direct reflections, which would yield a false response. The baffle between fiber and sample also helps prevent this.

Making use of two pinholes, to ensure only illuminating the sample, the overall intensity is much lower compared to the transmission measurements. Therefore, the exposure time is set to $120\,\mathrm{s}$ for three repetitions in accumulate mode for a sufficient intensity. To obtain the wavelength-dependent reflectivity for the spectrum of

¹⁴R12199 is the predecessor model of the mDOM PMT R15458. Except for minimal changes in geometry, all other relevant parts, especially PMT components, are believed to be identical.

¹⁵Newport 10D20AL.2.

 $\lambda = 250 \, \mathrm{nm}$ - $800 \, \mathrm{nm}$, two measurements are needed to cover the entire range. One measurement is taken in the range of $250 \, \mathrm{nm}$ - $570 \, \mathrm{nm}$ with grating G1 and the other in the range of $480 \, \mathrm{nm}$ - $800 \, \mathrm{nm}$ (G2).

Similarly to the transmission measurements (see section 4.3.1), three setup configurations are measured. The reference measurement (index r), where the light is incident on the mirror, the sample measurement (index s), where the first reflection occurs on the sample and a background measurement (index b). The last one is performed with a light trap which absorbs the collimated beam of the xenon lamp, but the light that is scattered in the collimation tube and released into the sphere at random angles is still measurable. This scattered light is present as a constant background in all measurements and hereby corrected. The reflectance is calculated based on eq. (3.2.2) as:

$$\rho_s(\lambda) = \rho_r(\lambda) \frac{L_s(\lambda) - L_b(\lambda)}{L_r(\lambda) - L_b(\lambda)}.$$
(4.4.1)

The reflectance of the reference mirror $\rho_r(\lambda)$ is provided by the manufacturer in [26]. Raw data exist for an angle of incidence (AOI) of 15° and 45° , both for s- and p-polarized light. In addition to that, plots are available with an AOI of 8° and unpolarized light, which matches the angle and light source used in the experiment. Because of that, the data for 8° was manually digitized via [27]. To account for the limited accuracy of this method, all reflectance values were given an absolute uncertainty of $\pm 1\,\%$. The data is interpolated for later usage,

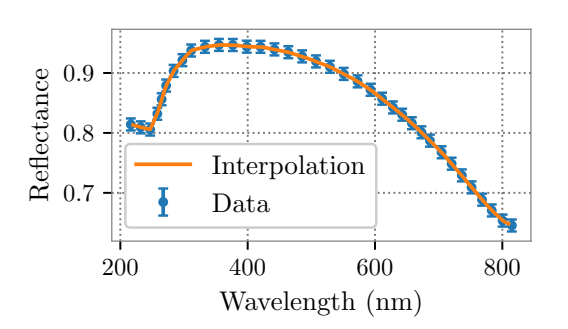


FIGURE 4.4.2: Raw reflectance data of the reference mirror with interpolation. Data extracted from [26].

as shown in fig. 4.4.2. For all results calculated by eq. (4.4.1), $\rho_r(\lambda)$ is obtained by this interpolation.

The results for the reflectance of the PMT components are shown in fig. 4.4.3. The raw data are processed as follows: For a single sample the reflectance is calculated with eq. (4.4.1). Then the reflectance is averaged in bins of 10 nm, calculating the standard error as uncertainty. Finally, the calculated reflectances for different samples of the same component are averaged. In fig. 4.4.3, the mean reflectance obtained here (labeled as new) is compared to the data taken in [6, p. 133] (labeled as old) by showing the residuals. An exception is the old data for the rectangular flaps. They were not measured previously, but instead set in simulation. As both datasets do not share common wavelengths, residuals are calculated via interpolation.

The bins in the new data are shifted one data point to the left as a direct consequence of the calibration (see section 4.2). Aside from this, the calibration does not have a striking impact. Since the calibration shifts the wavelengths, any impact would be noticeable in the characteristics of the reflectance curve, e.g. the minima of the reflectance curves of the dynode and the circular front plate. Based on the fit functions obtained in section 4.2, it would be expected to observe the minima slightly shifted to the left in the new measurements. This is not the case, which shows that the influence of the calibration is so small that it is covered up by other effects.

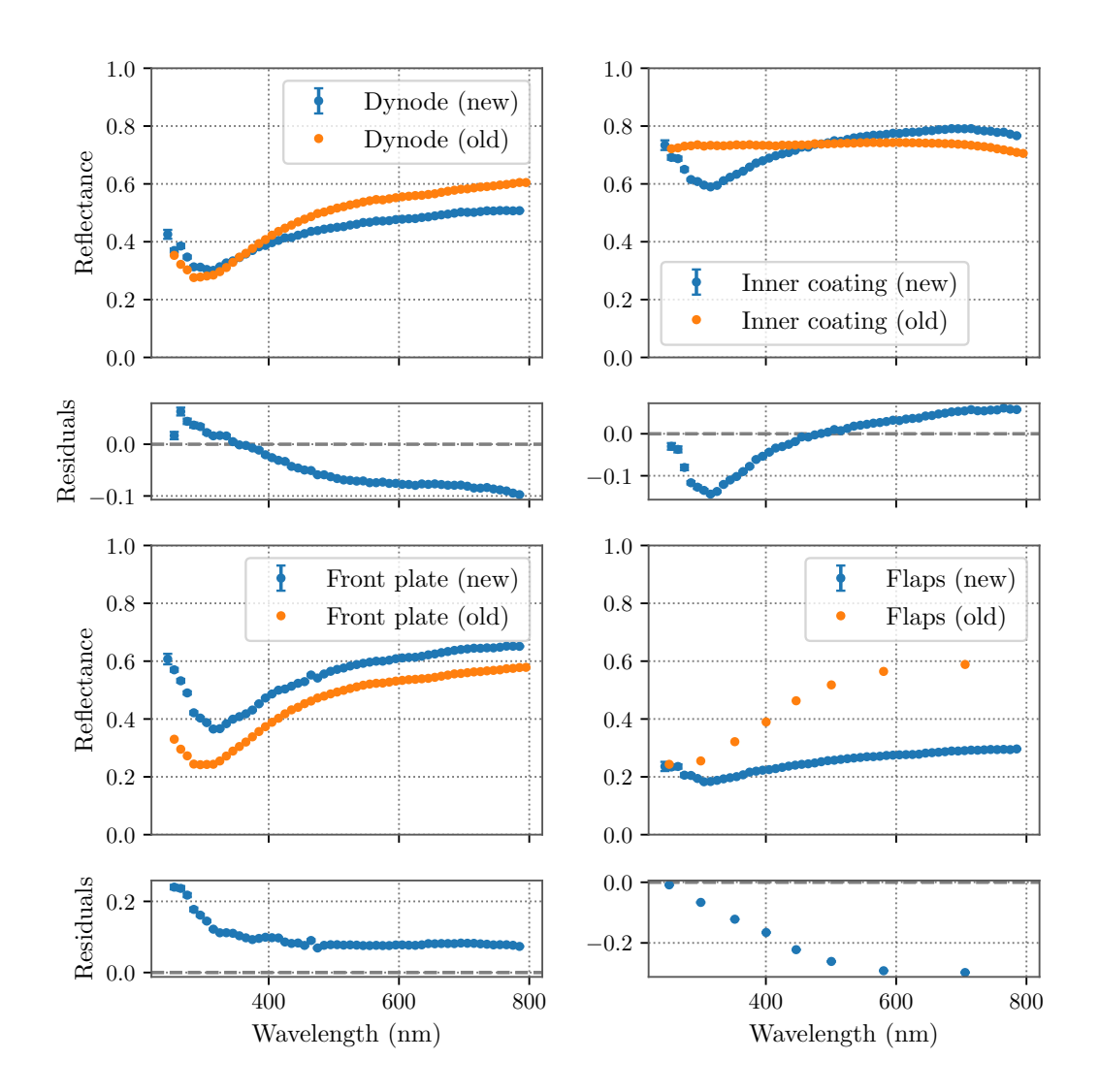


FIGURE 4.4.3: The results for mean reflectance of the measured PMT components are shown in blue (top left: dynode, top right: inner coating, bottom left: circular front plate, bottom right: rectangular flaps). In comparison, data of measurements made in [6, p. 133] are shown (orange). The old data for the rectangular flaps was not measured but set in simulation.

The results for the dynode show an analogical behavior between the old and new data, but the increase in reflectance after the minimum is distinctly smaller than in the old data and the difference in reflectance increases to (-0.0974 ± 0.0012) at $\lambda = 785 \, \mathrm{nm}$. For the circular front plate, both curves share the same characteristics, but reflectance in the new measurement is higher. After an initial difference of (0.2400 ± 0.0063) at $\lambda = 255 \, \mathrm{nm}$, the residuals decrease and stabilize for $\lambda > 480 \, \mathrm{nm}$ at ≈ 0.8 . The results for the inner coating are notable because they show changes in the characteristic of the curve. The old results display nearly constant reflectance throughout the wavelength range. This is not reproduced by the new data. Instead, characteristics similar to those seen for the dynode and front plate are observed.

To some extent, differences in reflectance can be expected because of the simple fact that samples from a different PMT were measured. However, since materials and

production are the same, observed deviations cannot be attributed solely to that. Reflection limitations could arise from damages and impurities that may be caused by extraction and transportation of the samples. However, these considerations cannot explain the different characteristics for the inner coating. Four different components showing the same characteristic suggest the assumption that there is a common material involved in all samples. In [6], it is stated that dynode and circular front plate are based on the same metal mixture. Whether the other components are also based on the same metal mixture is unclear. From visual confirmation alone, all components have noticeable differences in surface structure, even front plate and dynode (see also fig. 4.4.1). Another possibility could be remnants of the photocathode material on different components, causing a characteristic curve. One of the last steps of PMT production is the evaporation of the photocathode, released from capsules near the multiplication system [6]. If this process is sensitive in production, the amount of remnants may differ between two PMTs.

In addition, small variations in the measurement setup might explain some differences, as in [6] the sample was not mounted simultaneously during the reference measurement. This was made here to keep the average sphere reflectance constant (see section 3.2). However, the impact is presumably quite small due to the size of the sample with respect to the sphere size.

The reflectance of the rectangular flaps is lower than the values defined previously. This indicates that the assumption on which the values were chosen was wrong. However, because the flaps are so thin, they did not cover the whole cutout as opposed to the other sample measurements. As the mirror covers the whole cutout and the collimated beam is a little wider than the flaps, the illuminated area in the reference measurement might have been slightly larger, resulting in a higher intensity. This would lead to the conclusion that the real reflectance of the flaps is higher.

Since the measurement setup was expected to be practically isolated, measurements were taken with the low-intensity red room-lights on. However, some characteristics appeared initially in the raw intensity curves that were not present in previous measurements. Some simple tests were conducted to narrow down the source of external influence and it was found that the red light somehow seems to enter the spectrograph at some position, as the effect was eliminated when a blanket was placed over the spectrograph. These observations could be investigated further and should at least be considered when performing measurements with this setup. Henceforth, all measurements were taken in complete darkness and the ones that were taken before these observations were checked for these unwanted characteristics.

Because the samples were placed at a tilted angle, the integrating sphere integrates both specular and diffuse reflections, so the results present the total reflectance. The samples may be mounted at an angle of 0° to measure only the diffuse reflectance of the samples. In [6], studies were made with an adapted setup regarding the angular distribution of the reflected light. All samples showed some diffuse reflection, which is taken into account as surface roughness in the simulation [6]. For the evaluation of the simulated PMT sensitivity, which will be presented in the next chapter, the total reflectance values of the PMT components are updated. The newly introduced values are the mean of the old and new measurements to increase statistics.

5 Simulation of the PMT Response

In this chapter, the influence of the newly measured optical properties of internal components on the simulated PMT efficiency is investigated. Therefore, a brief introduction to the simulation framework Geant4¹⁶ is given. Introducing new values into the simulation requires a PMT matching, which is explained subsequently, whereupon the analysis of the PMT efficiency follows.

5.1 Geant4

Geant4 is a software toolkit for simulation of the passage of particles through matter. The open-source software is implemented in the object-oriented C++ programming language. The Monte-Carlo toolkit, originally developed for CERN and KEK, is under continuous development and used in a broad spectrum of scientific fields, such as particle and nuclear physics, accelerator design, medical physics and space engineering [28]. It provides all aspects necessary for the simulation of a particle physics experiment, such as its geometrical layout, the injection of particles into the experiment, the physical properties of used materials and the interactions between the injected particles and assigned materials. The defined detector volumes as well as particle trajectories can be visualized and the results can be extracted [28].

Geometry in Geant4 is based on building with primitive volumes such as cubes, cylinders, spheres or ellipsoids that can be further manipulated through boolean operations such as intersection, union or subtraction to create geometries of higher complexity. It is also possible to import volumes generated with CAD software [29]. Models are then built with a hierarchically structured geometry, placing one volume inside another.

Tracking in Geant4 works by propagating particles step by step through the simulation with a user-defined step size that optimizes the compromise between the performance of the execution and the required precision of the tracking. Successful simulation requires defining all material properties and specifying all particles as well as possible interactions in a physics list [28].

5.2 Simulating PMT Sensitivity with OMSim

OMSim is a Geant4-based framework, which is used to simulate PMTs and other optical modules of the IceCube Neutrino Observatory. For in-depth information, see the documentation in [24]. In this section, the models of a single mDOM-PMT and the complete mDOM are simulated before and after the introduction of the new reflectance values obtained in section 4.4. Changing values in the simulation requires

¹⁶GEometry ANd Tracking

a process called PMT matching, which is shown first. Afterwards, the results of effective area scans are presented, a core parameter to assess the sensitivity of PMTs and optical modules.

5.2.1 PMT Matching

Changing the optical properties of the materials of the PMT's internal components (see fig. 4.4.3) alters the PMT response, which must be corrected before investigating their impact on performance. In the simulation, each photon is assigned a weight corresponding to its detection probability. These weights are determined based on data files that are gradually generated throughout different steps with the module *efficiency_calibration* to match measurement data. For in-depth information, the reader is referred to [6, pp.135-143].

The old files concerning the PMT matching were deleted to start with the determination of the fraction of absorbed photons intrinsic to the simulation. In this step, the measurement setup for measuring QE is simulated. Based on the results, the quantum efficiency weights can be calculated. Now, the simulation that resembles the real experimental setup should yield a QE (see section 2.4) that matches the measured mean QE of an mDOM PMT. This step is run by simulating 500 000 photons for full wavelength coverage (250 nm - 795 nm in steps of 5 nm) and 5 000 000 photons for the low UV-region 250 nm - 300 nm for sufficient statistics. After introducing the file with new QE weights, the simulation is run again with 100 000 photons to verify if the weights were calculated properly. Plots of both steps are shown in fig. 5.2.1. It can be seen that the weights are calculated correctly as both curves now match well, which allows moving on to the next step.

In the next step, collection efficiency weights are calculated to match relative detection efficiency scans across the photosensitive region. These scans rasterize the

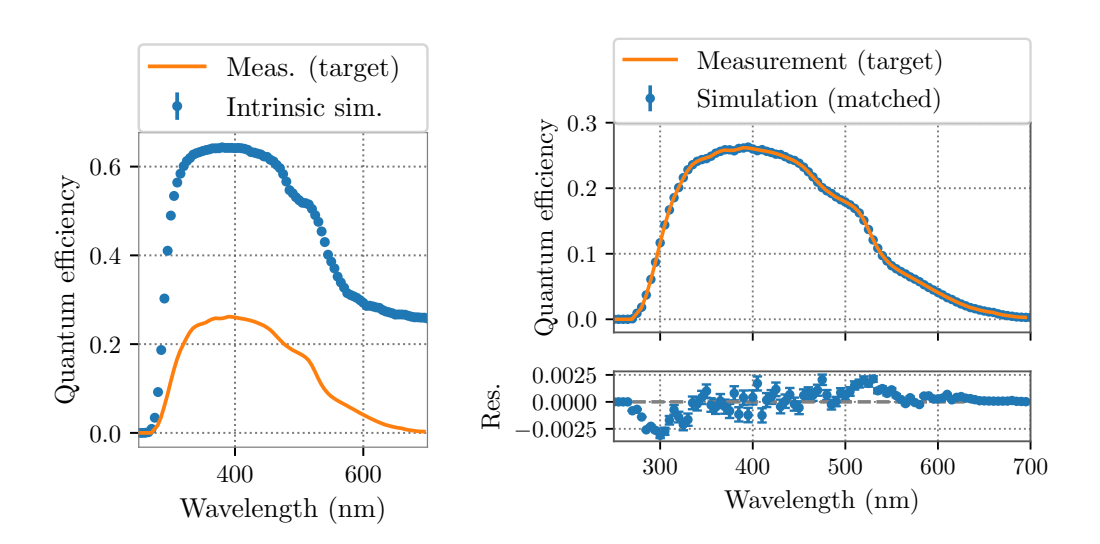


FIGURE 5.2.1: Left: Intrinsic simulation results of QE setup compared to measurement. Right: After calculating weights to match the target QE, a second simulation run yields the matching curves on the right.

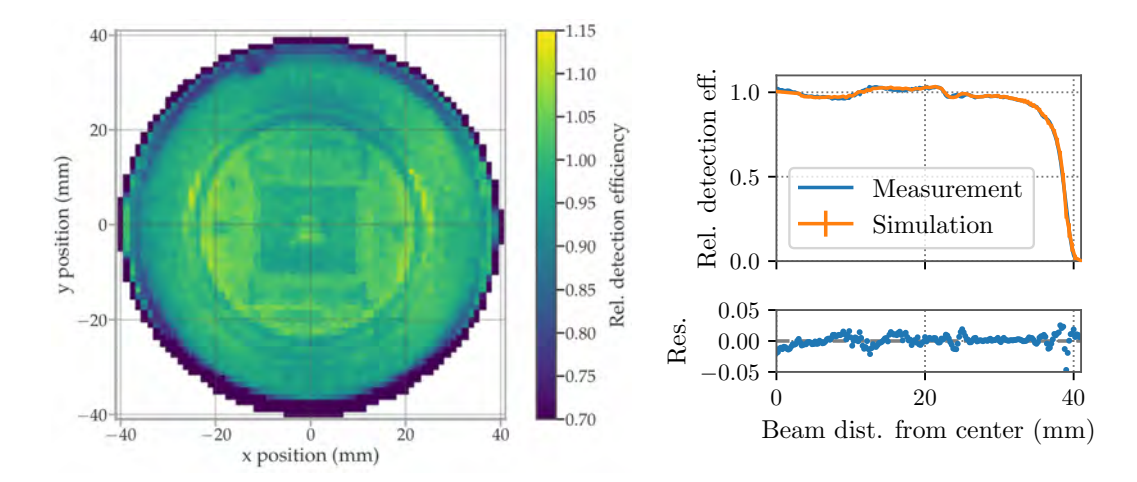


FIGURE 5.2.2: The relative detection efficiency scan shown on the left (taken from [6, p.90]) corresponds to the relative detection efficiency as a function of the beam distance from center, shown on the right. The simulation output matches the measurement after this matching step.

PMT in an x-y-grid. This is necessary to calculate weights for all different positions. In the previous steps, the QE for the entire photosensitive region was matched depending on wavelength. However, since the position of the incident photon has an impact on the detection efficiency because of different paths that photoelectrons have to take to reach the dynode, weights are also implemented for positions to account for local differences. This simulation step is run with 10 000 photons. For the positions, the weights can no longer be calculated with a simple fraction, so instead the weights are based on a fit model. If measurement and optimized fit match adequately, a file is generated with weights with respect to the distance R to the PMT center. The simulation is run again after importing the new weight file to check that the measurement and simulation match. This is shown in fig. 5.2.2: On the left, an x-y-scan of relative detection efficiency can be seen, which was measured in [6, p.90]. The x-y-data can be converted to the beam distance from the center, so the curve (labeled measurement) on the right corresponds to the scan on the left. It can be seen that the simulation with newly established weights works well, as the residuals, calculated in steps of 0.2 mm based on interpolations of both curves, are quite small.

In the last step, scan data of PMT characteristics are implemented. Therefore, an x-y-grid simulation is run with $100\,000$ photons and, based on the output, several files are created that assign positional dependence of PMT characteristics such as gain and transit time. After including these files, the matching process concludes with a final x-y-scan where $10\,000$ photons are simulated to verify the results for gain and transit time.

Before the PMT matching process, the same scan as this final scan from PMT matching was performed with the old values. The comparison of the results of these scans is shown in fig. 5.2.3. In addition, simulated scans are compared with measured scans with data taken from [6, p.142]. It can be seen that the measured scans show a smooth distribution for both gain (in PE units¹⁷) and transit time. The simulated scans, on the other hand, clearly show local differences, as the internal parts

¹⁷Represents the average charge produced by a **P**hoto**E**lectron after PMT multiplication [6].

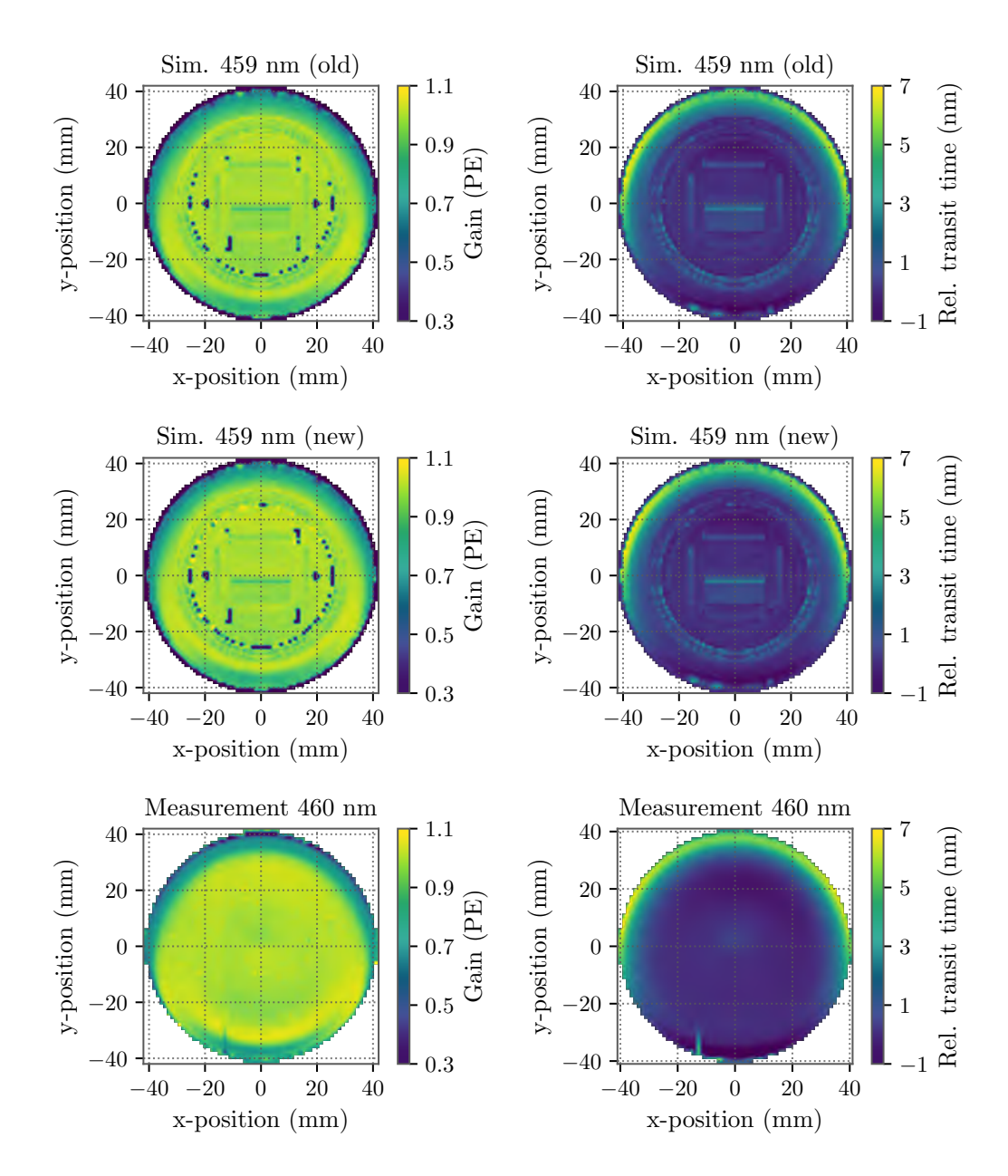


FIGURE 5.2.3: Comparison of gain (left) and relative transit time (right) scans before (old) and after (new) PMT matching, alongside measurement scans from [6, p.142].

are visible. However, the internal parts are already visible in the old simulated scans, which means that this effect has nothing to do with the introduction of new values and PMT matching. The explanation for the difference between simulation and measurement is justified by changes in simulation between the date of the scans here and the scans made in [6] and is not relevant for further discussion here. More importantly, the simulated scans for gain and transit time, respectively, yield quite similar results. Local differences for single pixels may be attributed to statistics in simulation. The comparable results show that PMT matching was performed correctly and that no unwanted side effects were instituted. The establishment of new reflectance values should not change these scans regarding gain and transit time. Instead, they may have an influence on effective area scans, which are presented in the following.

5.2.2 Effective Area Scans

The effective area is a core parameter for the characterization of the sensitivity of optical modules and their angular acceptance. In the following sections, effective area scans are executed on a single PMT and an entire mDOM. Therefore, the module AngularScan is performed, simulating a disk that emits mono-energetic photons perpendicular with a uniform density profile [14] (see fig. 5.2.4 for the simulated PMT and mDOM model). The effective area $A_{\rm eff}(\theta,\phi)$ represents the area that is detected from a plane wave of incidence angle of θ (zenith) and ϕ (azimuth) with respect to the coordinate origin specified for the module. The effective area for a particular direction of the incident wave is calculated as

$$A_{\text{eff}}(\theta, \phi) = \frac{N_{\text{det}}(\theta, \phi)}{N} \cdot A_{\text{rad}}, \tag{5.2.1}$$

where N denotes the number of simulated photons, $N_{\rm det}$ is the number of photons that are detected and $A_{\rm rad}$ represents the area of the disk emitter [14]. The radius of the disk emitter can be set for the angular scan and has to be larger than the projected cross section of the PMT model in any direction. Furthermore, there must be no overlap between emission disc and PMT volume, which is why a distance is set for the scan. Both values can be optimized via the visualizer. To characterize the overall sensitivity, the disk emitter is *rotated* around the PMT for 4π solid angle coverage. The distance and angles are set with respect to the coordinate origin at the middle of the photocathode's end (see fig. 5.2.4). To achieve optimal angular coverage, n angle pairs are chosen using the healpy package [30] which separates the spherical surface into n pixels of equal area. Thus, the mean effective area is defined as [6]:

$$\overline{A}_{\text{eff}} = \frac{1}{n} \sum_{i=1}^{n} A_{\text{eff}}(\theta_i, \phi_i). \tag{5.2.2}$$

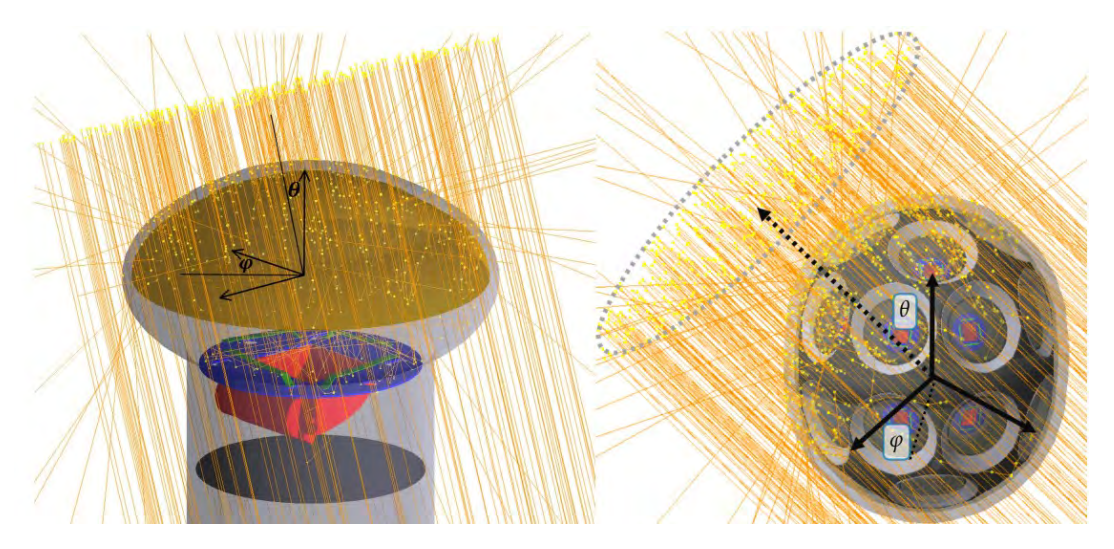


FIGURE 5.2.4: Screenshots of the PMT (left) and mDOM model (right) in the Geant4 visualizer. The model is illuminated by photons emitted from a disk, simulating a plane wave from the direction (θ, ϕ) . Trajectories are indicated by yellow lines, physical interactions are shown with yellow dots. The picture on the right is taken from [6].

Single PMT

For the results presented in the following, the same simulation is performed on a single PMT before and after importing the new reflectance values. The wavelength range 250 nm - 720 nm is covered in steps of 10 nm. For each wavelength, 768 angle pairs are generated and for each angle pair, 250 000 photons are simulated. It is possible to simulate different environments like air (used here and for the mDOM in the next section) or ice. With the simulation results, the mean effective area is calculated via eq. (5.2.2). The comparison of both mean effective areas is shown in fig. 5.2.5. It should be mentioned that during PMT matching, new QE values were matched. The QE values that were used before were the mean between old (R12199) and new PMTs (R15458). However, effective area measurements of an mDOM made in [31] show better agreement with the OE curve of R15458, which is reasonable and why this QE curve was matched here. This causes an additional source of differences in comparison of the mean effective area results with old data. To rule out this effect, the simulation results with the new values are corrected in post by multiplying them with the ratio of old to new QE values. In this way, only the differences caused by the new reflectance values can be assessed.

It can be seen that towards the edges $250~\rm nm$ and $720~\rm nm$, the mean effective area approaches zero, which does not differ between both simulations. This reflects the QE that was matched in fig. 5.2.1, as the QE approaches zero on both ends. Between that, the mean effective area after implementing the new reflectivities shows smaller values for lower wavelengths, the residuals reach a minimum at $\lambda = 340~\rm nm$, but increase for $\lambda > 450~\rm nm$ peaking at $\lambda = 560~\rm nm$. The residuals show a behavior quite similar to the residuals for the reflectance of the inner coating (see fig. 4.4.3). On first notice, it might seem reasonable that a lower reflectance should result in a lower mean effective area and vice versa because it is less (more) likely that a photon that was transmitted at first is still detected as it crosses the photocathode again. However, this was taken into account when matching the QE curve. The crucial point is that the QE measurement and its simulation only considers a frontal

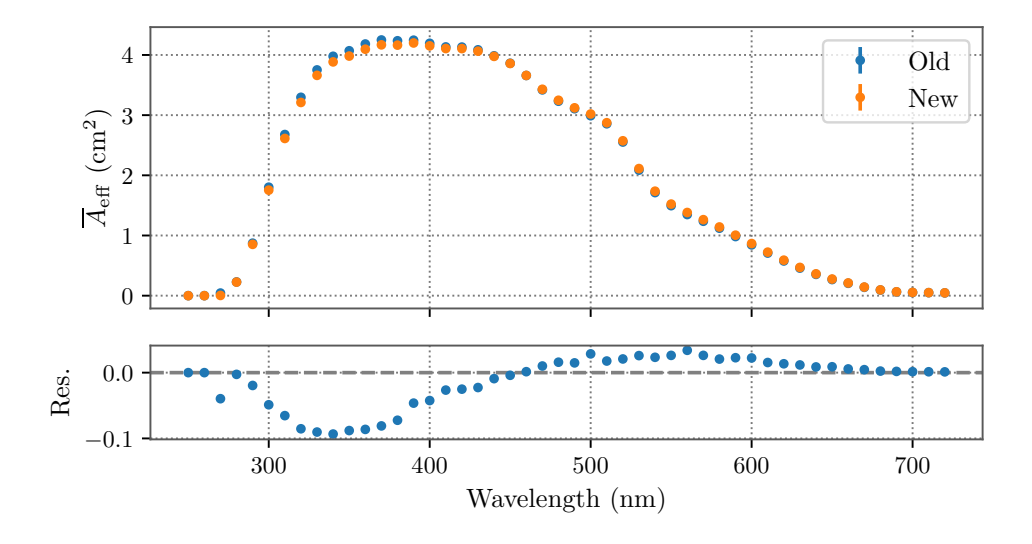


FIGURE 5.2.5: Comparison of the mean effective area for a single PMT before (old) and after (new) introduction of new reflectance values.

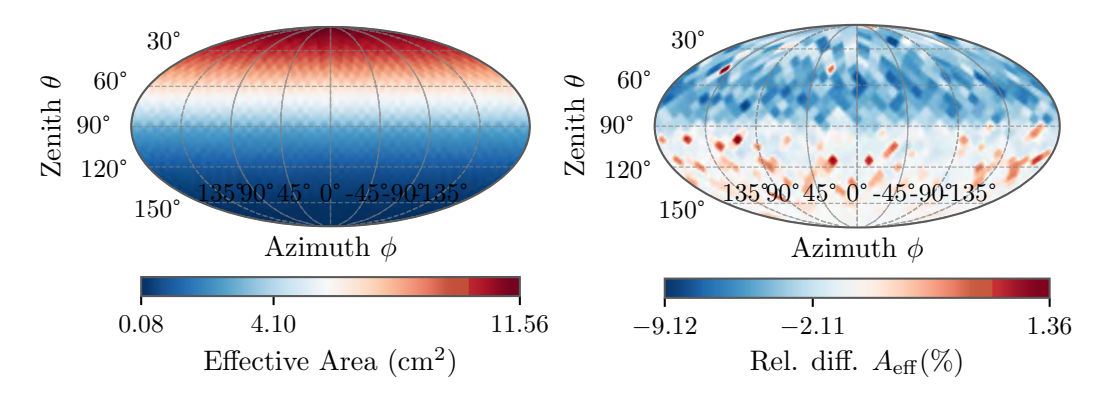


FIGURE 5.2.6: Left: Local effective area for a single PMT at $\lambda = 360\,\mathrm{nm}$ after matching. Right: Relative local differences in effective area before and after introduction of new reflectance values. Calculated via $(A_{\mathrm{eff,new}} - A_{\mathrm{eff,old}})/\overline{A}_{\mathrm{eff,new}}$.

beam. Since the effective area scan illuminates the PMT from all directions, photons are also incident on the entry window at an angle. In this regard, the importance of the inner coating becomes clear, as it is more likely that transmitted photons hit the inner coating because parts of the other internal components have a significantly lower probability of being illuminated towards flatter angles. These considerations imply why the residual curve resembles those of the inner coating and not those of the rectangular flaps, for example, which show larger differences in reflectance but are distinctly smaller than those of the inner coating and less likely to be hit at flat incident angles.

On the left side of fig. 5.2.6, an effective area scan is shown with respect to the angle of incidence (θ,ϕ) (see eq. (5.2.1) for the calculation) for $\lambda=360\,\mathrm{nm}$. The plot on the right shows the local change in effective area, calculated by subtracting the old effective area from the new effective area (plot on the left) and dividing the result by the new mean effective area. Once again, as mentioned above, the new effective area is corrected for by the ratio of old and new QE values.

The plot reveals that the new mean effective area is 2.11 % smaller than the old one for $\lambda = 360 \,\mathrm{nm}$, which corresponds to the value of fig. 5.2.5, when the residual is divided by the new mean effective area at $\lambda = 360\,\mathrm{nm}$. This wavelength was chosen for this plot, because it was among the wavelengths with the largest residuals in fig. 5.2.5. In general, the difference in mean effective area is between $(-2.402 \pm$ 0.042)% and $(2.457 \pm 0.050)\%$. Regarding local differences, the most apparent observation can be made for $30^{\circ} < \theta < 90^{\circ}$, where the largest deviations occur, reaching relative differences of up to -9.12%. These angles represent incoming photons from above the PMT at flat angles (see fig. 5.2.4 for coordinate definition). Therefore, these results support the hypothesis made earlier that the inner coating plays the most important role for these angles because the first matching step sets the QE for $\theta = 0^{\circ}$, but for the discussed θ -values, the inner coating is mainly illuminated. For $\theta > 90^{\circ}$, the photons hit the PMT bulb from below and the effective area is low (see left side of fig. 5.2.6). Accordingly, no noticeable local differences are to be expected and the small deviations that are observable can be attributed to statistical fluctuations.

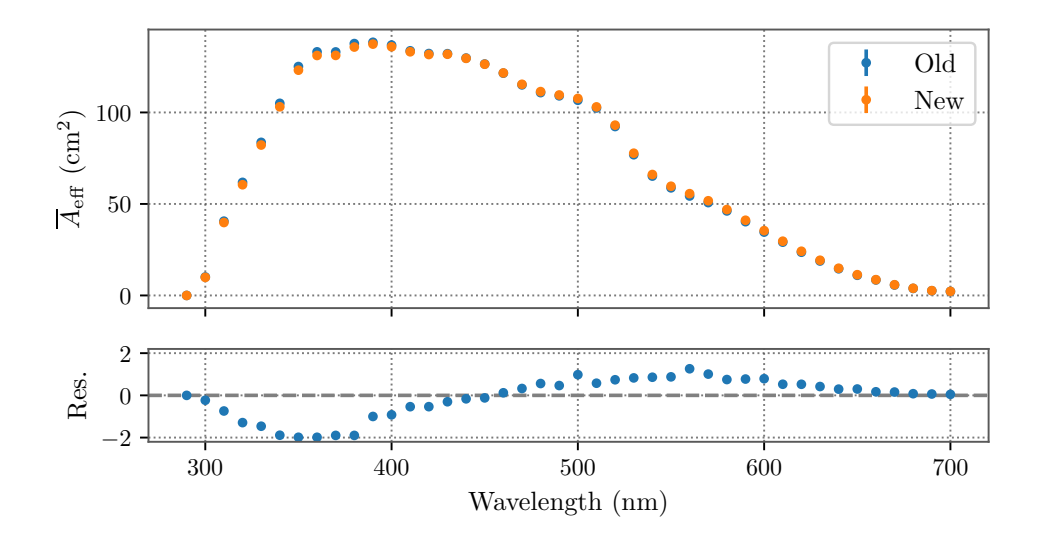


FIGURE 5.2.7: Comparison of the mean effective area of the mDOM before (old) and after (new) introduction of new reflectance values.

mDOM

Similar evaluations are also made for the mDOM (see section 2.3), which houses 24 PMTs. Here, simulations are run with 100 000 photons in steps of 10 nm in the range 290 nm - 700 nm. Once again, 768 angle pairs are generated. The simulation output contains all the data needed to determine the mean effective area for the entire module as well as for each individual PMT. With the same reasoning as before, the ratio of the QE values is included in all results presented in the following, to solely evaluate the differences arising out of the new reflectance values.

In fig. 5.2.7, the mean effective area for the entire mDOM is shown. The absolute values are not simply twenty-four times the results of the single PMT as increased photon collection by reflectors and shadowing by the holding structure impact overall sensitivity. Furthermore, everything is enclosed in a pressure vessel whose transparency is quite small for $\lambda < 300\,\mathrm{nm}$ (see also fig. 4.3.3) explaining why the mean effective area of the mDOM already approaches zero for $\lambda = 290\,\mathrm{nm}$. The residuals show a behavior similar to the results of the single PMT. Since the PMTs of the mDOM are arranged uniformly in all directions, providing near-homogeneous angular acceptance [14], it makes sense that the characteristics of the mDOM's mean effective area reflect those of the single PMT.

On the left side of fig. 5.2.8, the difference of the mean effective area is evaluated separately for all polar and all equatorial PMTs of the mDOM. Therefore, the mean effective area is calculated for every single PMT by eq. (5.2.1) and then averaged over all polar and equatorial PMTs, respectively. Finally, the plot shows the difference between new and old simulation. It can be found that there is no deviancy between polar and equatorial PMTs. On the right side of fig. 5.2.8, a plot of relative local differences is shown for $\lambda = 360\,\mathrm{nm}$. It can be seen that the relative difference in the effective area is $-1.514\,\%$ on average, which is smaller than the PMT value $(-2.11\,\%)$. In general, the new mean effective area shows deviation between

¹⁸The PMTs at the top and at the bottom of the mDOM are often referred to as polar PMTs, whereas the other 16 PMTs are called equatorial PMTs. See fig. 5.2.4 for an illustration of the mDOM model.

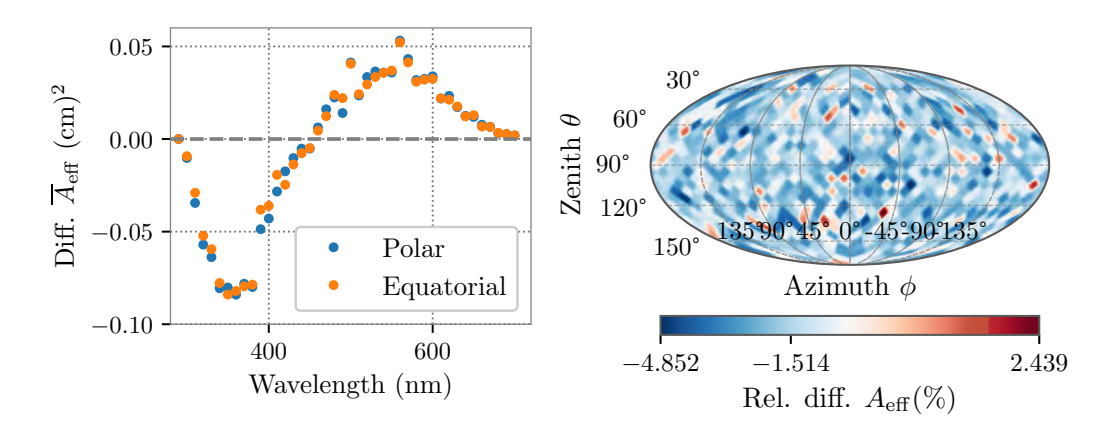


FIGURE 5.2.8: Left: Comparison of the difference in mean effective area for polar and equatorial PMTs. Right: Relative local differences in effective area for the mDOM at $\lambda = 360\,\mathrm{nm}$.

 (-1.613 ± 0.044) % and (2.266 ± 0.047) %. The highest deviation locally in fig. 5.2.8 is -4.852 %, while it is -9.12 % for the PMT. Overall, no local characteristics stand out, which is to be expected due to the design of the mDOM. A simulation with more statistics and even more generated angle pairs for more pixels may yield even clearer comparison maps by reducing statistical fluctuations. This accounts for the maps of the local effective area differences for both the single PMT and the mDOM.

Overall, the considerations made here for the single PMT and the mDOM show a small but noteworthy impact by the newly measured reflectance values of the internal PMT components in section 4.4. Based on the similarities of the residuals, the hypothesis is made that the new values of the inner coating are (for the most part) responsible for the change in mean effective area. However, although some reflectance results may seem quite noticeable (e.g., rectangular flaps alongside inner coating), the absolute deviations of the new mean effective area do not exceed $(2.457 \pm 0.050)\%$ (PMT) and $(2.266 \pm 0.047)\%$ (mDOM). Nonetheless, these new values are not too small to be neglected and may be considered in optical module sensitivity studies because the internal component material definitions are also used for other PMT types.

6 Summary and Outlook

This thesis aimed to characterize the optical properties of internal PMT components, with a particular focus on their reflectance. Similar measurements were made in [6] and serve as a baseline for the results of this thesis. The initial motivation for the renewed measurements was a lack of calibration of the spectrometer in [6]. Using a calibration lamp, two wavelength calibration functions were successfully determined in section 4.2 that allow an accuracy of $< 1\,\%$ deviation. They can be applied to data post-measurement and therefore used in future measurements for any setup including the spectrometer. The calibration resulted in an effective wavelength shift between $(-3.56\pm0.49)\,\mathrm{nm}$ and $(-6.50\pm0.48)\,\mathrm{nm}$, implying only a minor impact on subsequent measurements.

First, transmission measurements with optical bandpass filters in section 4.3.1 confirmed the accuracy of the calibration, as the bandpasses were shifted close to their given center wavelengths. In addition to that, the bandwidth specifications (10 ± 2) nm were confirmed and the transmission stated by the manufacturer was mostly verified (except for F310). The blocking quality of the filters could not be validated, which is ascribed to limitations of the setup. For adequate validation, a setup that is more capable of measuring the UV region around $250\,\mathrm{nm}$ would be needed.

For the reflectance of the PMT components, the impact of the calibration is so small that it is overshadowed by broader differences. The findings shown in section 4.4 for the dynode, front plate and inner coating show differences in absolute reflectance compared to data taken in [6]. The inner coating shows the most notable observation, with its curve shifting from a nearly constant trend to a trend similar to that of the other components. Possible explanations include that small variations between different PMTs can be expected and that the photocathode evaporation process might leave residues on internal components. It might be interesting to measure even more samples from other PMTs to increase statistics and check the reflectance curve for the inner coating. The rectangular flaps that were measured for the first time show a reflectance significantly lower than the values that were set in the simulation. This could indicate an overestimation of the previous values, even though another assumption was made suggesting that the illuminated area of the sample and the reference were slightly different. This does not pose a problem because the impact of the flaps is small due to their size, but it could be verified by restricting the diameter of the beam even further and ensuring that the bracket cutouts allow for the same illuminated area.

The reflectance values set in the simulation material files were then updated with the average of the new and old values (see section 5.2). Subsequently, after a successful PMT matching, effective area scans on the single PMT and the mDOM revealed the impact of the updated reflectivity values of the internal components. Both residual curves from the comparison of the new and old mean effective areas show a behavior similar to the residual curve of the reflectance measurement of the inner coating, leaving the supposition that the inner coating is mainly responsible for changes in effective area. This is supported by the fact that the inner coating covers a large area that is primarily illuminated towards flatter angles. The local relative differences in fig. 5.2.6 uphold this further, as the highest deviations appear in $30^{\circ} < \theta < 90^{\circ}$. In general, the change in the mean effective area is between $(-2.402 \pm 0.042) \%$ and $(2.457 \pm 0.050) \%$ for the single PMT and between $(-1.613 \pm 0.044) \%$ and $(2.266 \pm 0.047) \%$ for the mDOM depending on wavelength.

Overall, the introduction of updated optical properties was successful and, although small, may be considered in future studies on the PMTs and mDOM. In addition to the new reflectance values, new QE values were matched, which was a required update for OMSim, and was conveniently updated during the performed matching. Other studies on the mDOM, such as simulations on background rates induced by radioactive decays, should be repeated with the updated values. Lastly, in OMSim, PMTs of different optical modules, such as the DOM, rely on the updated material files and therefore require re-matching (see section 5.2.1) as well.

A Appendix

Measurement of the Calibration Lamp in Image Mode

If the measurement is taken as a full-resolution 2D raw image, the output of the software can be visualized as fig. A.0.1. In this colormap, yellow colors correspond to high intensities of the calibration lamp. Toward the top and bottom of the plot, the lines bend slightly, which explains the *shoulder* of the peaks (see fig. 4.2.2) after transformation to a 2D spectrum.

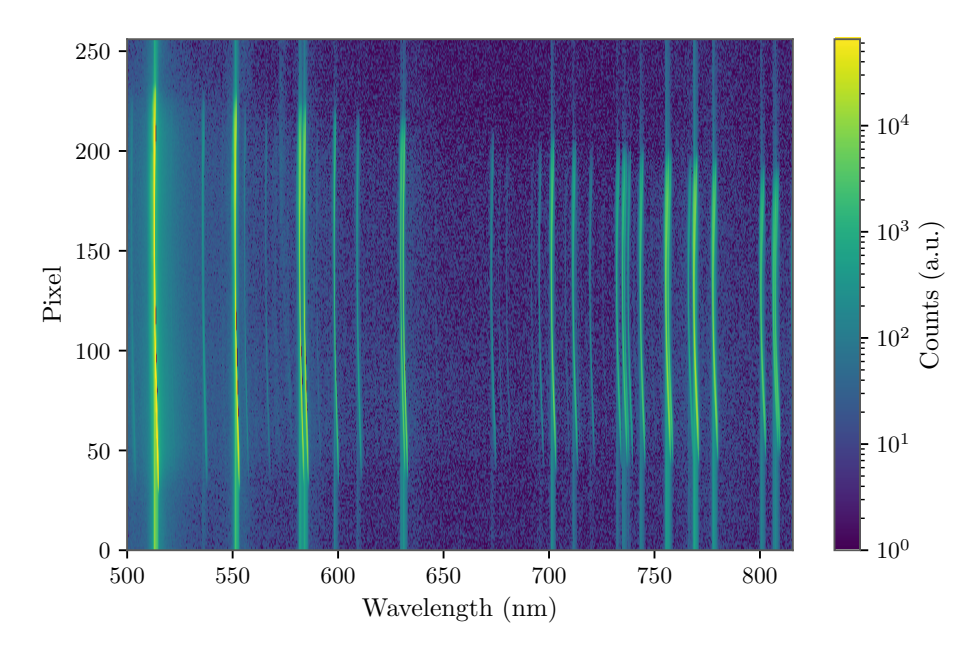


FIGURE A.0.1: Color map of a calibration lamp measurement. The horizontal axis shows wavelength (internally converted from CCD pixels), while vertical intensity lines represent characteristic spectral features.

Transmission Measurements of the Filters with the Comparison Method

The transmittance results for the bandpass filters shown in section 4.3.1 are ideally calculated, although the sample was simply switched with the empty entrance port. This means the average sphere reflectance was not the same. After using the comparison method (see section 3.2) for the reflectance measurements, the measurements for the filters were taken again with the comparison method. Now, light can leave the sphere through an additional empty port in the transmission measurement and through a port equipped with a filter in

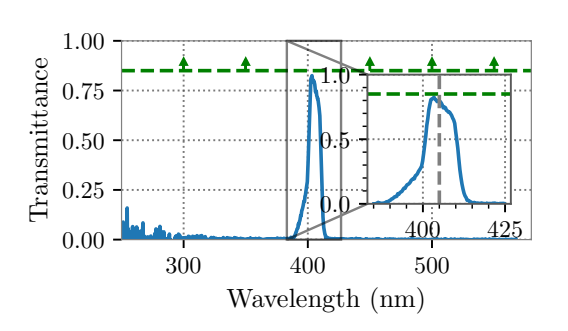


FIGURE A.0.2: Transmittance of bandpass filter F405. Measured with the comparison method.

the reference measurement. Therefore, for the bandpass region, only minor losses in transmittance are expected due to the small size of the port and the fact that the intensity loss in the reference measurement is assumed to just be slightly smaller than in the transmission measurement because the reflectance of the filter is low. However, the results in figs. A.0.2 and A.0.3 show differences greater than expected along with other effects. As per these results, none of the filters achieve the required transmittance. Additionally, F405, F365 and F337 now show a left *shoulder* and an imbalance in the peak structure, as transmittance is higher for the lower end of their bandwidth and decreases distinctly throughout the band. These two effects cannot be attributed to the comparison method, which is why the results are not considered reliable enough to replace those shown in section 4.3.1.

Manufacturer Specifications of Bandpass Filters

The specifications given by the manufacturer regarding the bandpass filters presented in section 4.3.1 can be found in table A.0.1 sorted by their center wavelength (CWL).

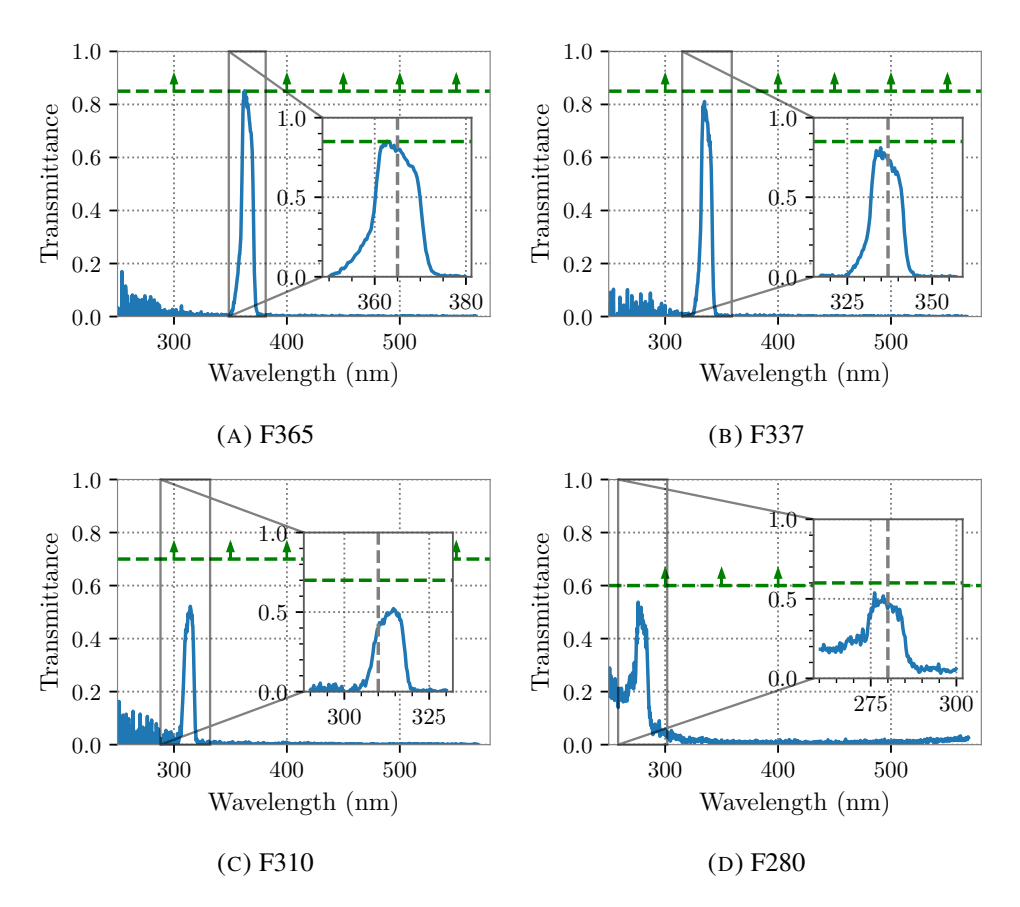


FIGURE A.0.3: Transmittance results for other filters, measured with the comparison method.

TABLE A.0.1: Specifications given by the manufacturer of the bandpass filters.

CWL	FWHM	Transmission	Blocking
$(280 \pm 2) \text{nm}$	$(10\pm2)\mathrm{nm}$	> 60 %	>OD4 abs: 220 nm - 265 nm & 298 nm - 320 nm
			>OD4 avg: 320 nm - 650 nm
$(310 \pm 2) \text{nm}$	$(10\pm2)\mathrm{nm}$	> 70 %	>OD3 abs,
			>OD4 avg: 200 nm - 295 nm & 325 nm - 1200 nm
$(337 \pm 2) \text{nm}$	$(10 \pm 2) \mathrm{nm}$	> 85 %	>OD3 abs,
			>OD4 avg: 200 nm - 322 nm & 352 nm - 1200 nm
$(365 \pm 2) \text{nm}$	$(10 \pm 2) \mathrm{nm}$	> 85 %	>OD3 abs,
			>OD4 avg: 200 nm - 1200 nm
$(405 \pm 2) \text{nm}$	$(10 \pm 2) \mathrm{nm}$	> 85 %	>OD3 abs,
			>OD4 avg: 200 nm - 1200 nm

Comparison of the mDOM mean effective Area without correcting by the QE Ratio

In fig. A.0.4, the ratio QE_{old}/QE_{new} is shown that was multiplied by the new (mean) effective area to correct the results presented in section 5.2. In fig. A.0.5 the mean effective area comparison for the mDOM is shown without correcting the QE ratio. It can be seen that the residuals increase noticeably and exhibit a different behavior at higher wavelengths, where the new mean effective area is lower. This indicates that the overall mDOM effective area decreases as a result of the updated, more realistic QE curve. Furthermore, this shows that it was well justified to correct the new results using the QE ratio to solely evaluate effects introduced by the new reflectance values.

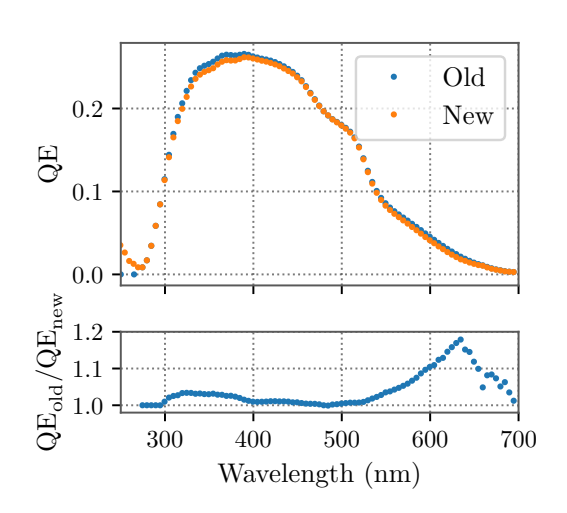


FIGURE A.0.4: Comparison of old (Mean of R12199 and R15458) and new (R15458) QE.

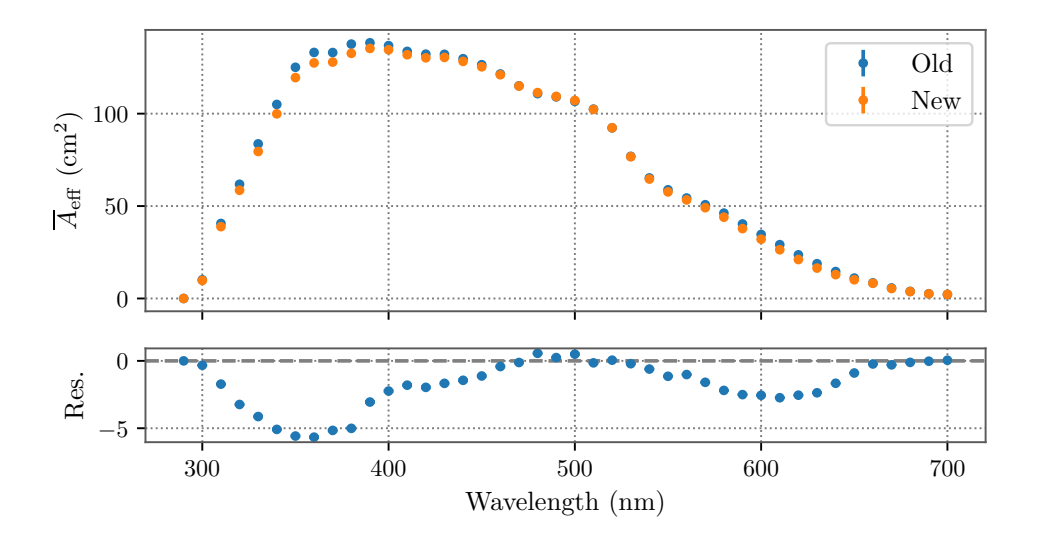


FIGURE A.0.5: Comparison of the mean effective area of the mDOM without accounting for the new QE values.

Bibliography

- [1] C. Grupen. *Astroparticle physics*. Berlin: Springer, 2005. ISBN: 978-3-540-25312-9.
- [2] M.G. Aartsen et al. "The IceCube Neutrino Observatory: instrumentation and online systems". In: Journal of Instrumentation 12.3 (Mar. 14, 2017), P03012–P03012. ISSN: 1748-0221. DOI: 10.1088/1748-0221/12/03/P03012. URL: https://iopscience.iop.org/article/10.1088/1748-0221/12/03/P03012.
- [3] The IceCube-Gen2 Collaboration et al. "IceCube-Gen2: The Window to the Extreme Universe". In: *Journal of Physics G: Nuclear and Particle Physics* 48.6 (June 1, 2021), p. 060501. ISSN: 0954-3899, 1361-6471. DOI: 10.1088/1361-6471/abbd48. URL: http://arxiv.org/abs/2008.04323.
- [4] IceCube Collaboration et al. "First observation of PeV-energy neutrinos with IceCube". In: *Physical Review Letters* 111.2 (July 8, 2013), p. 021103. ISSN: 0031-9007, 1079-7114. DOI: 10.1103/PhysRevLett.111.021103. URL: http://arxiv.org/abs/1304.5356.
- [5] A. Ishihara. The IceCube Upgrade Design and Science Goals. Aug. 26, 2019. DOI: 10.48550/arXiv.1908.09441. URL: http://arxiv.org/abs/1908.09441.
- [6] M. A. Unland Elorrieta. "Development, simulation, and characterisation of a novel multi-PMT optical module for IceCube Upgrade with emphasis on detailed understanding of photomultiplier performance parameters". PhD thesis.

 Universität Münster, 2023. URL: https://www.uni-muenster.de/imperia/md/content/physik_kp/agkappes/abschlussarbeiten/doktorarbeiten/phd_thesis_unland.pdf.
- [7] L. Oberauer and J. Oberauer. *Neutrinophysik: Grundlagen, Experimente und aktuelle Forschung.* 1. Aufl. 2019. Berlin, Heidelberg: Springer Berlin Heidelberg, 2019. ISBN: 978-3-662-59335-6. DOI: 10.1007/978-3-662-59335-6.
- [8] KATRIN Collaboration† et al. "Direct neutrino-mass measurement based on 259 days of KATRIN data". In: Science 388.6743 (Apr. 11, 2025), pp. 180– 185. ISSN: 0036-8075, 1095-9203. DOI: 10.1126/science.adq9592. URL: https://www.science.org/doi/10.1126/science.adq9592.
- [9] J. A. Formaggio and G. P. Zeller. "From eV to EeV: Neutrino Cross Sections Across Energy Scales". In: *Reviews of Modern Physics* 84.3 (Sept. 24, 2012), pp. 1307–1341. ISSN: 0034-6861, 1539-0756. DOI: 10.1103/RevModPhys. 84.1307. URL: http://arxiv.org/abs/1305.7513.

Bibliography 40

[10] M. A. Unland Elorrieta. "Studies on dark rates induced by radioactive decays of the multi-PMT digital optical module for future IceCube extensions". Master's Thesis. Münster: Univerität Münster, 2017. URL: https://www.uni-muenster.de/imperia/md/content/physik_kp/agkappes/abschlussarbeiten/masterarbeiten/1712-ma_munland.pdf.

- [11] W. Demtröder. *Experimentalphysik 4*. Springer-Lehrbuch. Berlin, Heidelberg: Springer Berlin Heidelberg, 2017. ISBN: 978-3-662-52884-6. DOI: 10.1007/978-3-662-52884-6. URL: http://link.springer.com/10.1007/978-3-662-52884-6.
- [12] IceCube Collaboration. *IceCube Detector*. URL: https://icecube.wisc.edu/science/icecube/(visited on 06/15/2025).
- [13] IceCube Collaboration et al. "IceTop: The surface component of IceCube". In: Nuclear Instruments and Methods in Physics Research Section A: Accelerators, Spectrometers, Detectors and Associated Equipment 700 (Feb. 2013), pp. 188–220. ISSN: 01689002. DOI: 10.1016/j.nima.2012.10.067. URL: http://arxiv.org/abs/1207.6326.
- [14] L. Classen. "The mDOM a multi-PMT digital optical module for the IceCube-Gen2 neutrino telescope". PhD thesis. FAU Erlangen-Nürnberg, 2017. URL: https://www.uni-muenster.de/imperia/md/content/physik_kp/agkappes/abschlussarbeiten/doktorarbeiten/1702-phd_lclassen.pdf.
- [15] Hamamatsu Photonics K.K. *Photomultiplier tubes Basics and Applications*. 4th ed. 2017. URL: https://www.hamamatsu.com/content/dam/hamamatsu-photonics/sites/documents/99_SALES_LIBRARY/etd/PMT_handbook_v4E.pdf (visited on 09/13/2025).
- [16] M. Dittmer. Private communication.
- [17] A. G. Wright. *The Photomultiplier Handbook*. Vol. 1. Oxford University Press, Aug. 24, 2017. ISBN: 978-0-19-956509-2. DOI: 10.1093/oso/9780199565092. 001.0001. URL: https://academic.oup.com/book/27426.
- [18] Labsphere. Integrating Sphere Theory and Applications. 2017. URL: https://www.labsphere.com/wp-content/uploads/2021/09/Integrating-Sphere-Theory-and-Applications.pdf (visited on 07/01/2025).
- [19] MKS Instruments. Spectralon Collimated Beam Integrating Spheres. 2020. URL: https://www.newport.com/medias/sys_master/resources/hfb/h29/9954239840286/DS-050620%20819C%20Series%20Spectralon%20Spheres%20Datasheet/DS-050620-819C-Series-Spectralon-Spheres-Datasheet.pdf (visited on 07/01/2025).
- [20] Thorlabs. THORLABS M114L01. URL: https://www.thorlabs.com/thorproduct.cfm?partnumber=M114L01 (visited on 09/13/2025).

Bibliography 41

[21] Oxford Instruments. Andor Kymera 193i Intelligent, Modular and Compact Spectrograph for Physical and Life Science. URL: https://andor.oxinst.com/assets/uploads/products/andor/documents/andor-kymera-193-specifications.pdf (visited on 07/09/2025).

- [22] Oxford Instruments. Andor Newton CCD Spectroscopy at Pace. URL: https://andor.oxinst.com/assets/uploads/products/andor/documents/andor-newton-ccd-specifications.pdf (visited on 07/09/2025).
- [23] Andor Technology. *User's Guide To The: Andor Technology newton*. Aug. 2008. URL: https://www.tokyoinst.co.jp/product_file/file/AD01_man01_ja.pdf (visited on 07/20/2025).
- [24] *OMSim Geant4 Framework*. URL: https://icecube.github.io/OMSim/(visited on 08/15/2025).
- [25] W. Demtröder. *Experimentalphysik 2: Elektrizität und Optik.* 7. Aufl. 2017. Springer-Lehrbuch. Berlin, Heidelberg: Springer Berlin Heidelberg, 2018. ISBN: 978-3-662-55790-7. DOI: 10.1007/978-3-662-55790-7.
- [26] Newport. *UV Aluminum Mirror*. URL: https://www.newport.com/p/10D20AL.2 (visited on 08/25/2025).
- [27] A. Rohatgi. WebPlotDigitizer. Version 3.4. URL: https://automeris.io/WebPlotDigitizer (visited on 09/13/2025).
- [28] S. Agostinelli et al. "Geant4—a simulation toolkit". In: *Nuclear Instruments and Methods in Physics Research Section A: Accelerators, Spectrometers, Detectors and Associated Equipment* 506.3 (July 2003), pp. 250–303. ISSN: 01689002. DOI: 10.1016/S0168-9002(03)01368-8. URL: https://linkinghub.elsevier.com/retrieve/pii/S0168900203013688.
- [29] C. M. Poole et al. "A CAD interface for GEANT4". In: *Australasian Physical & Engineering Sciences in Medicine* 35.3 (Sept. 2012), pp. 329–334. ISSN: 0158-9938, 1879-5447. DOI: 10.1007/s13246-012-0159-8. URL: http://link.springer.com/10.1007/s13246-012-0159-8.
- [30] healpy documentation. URL: https://healpy.readthedocs.io/en/latest/(visited on 08/15/2025).
- [31] M. A. Unland Elorrieta, A. Kappes, and A. Franckowiak. "Preliminary measurements of mDOM sensitivity in air". Unpublished. 2024.

Acknowledgements

First of all I would like to express my gratitude to Prof. Alexander Kappes for providing me with the opportunity to write this thesis in his working group. I wish to extend my gratitude to Dr. Volker Hannen for being my second examiner.

Special thanks go out to my supervisors, Berit Schlüter and Markus Dittmer, for your help in the lab, for your advice and proofreading of my thesis. Thank you very much for always taking the time to answer all my questions.

I want to thank the whole working group for creating a fun-filled and kind work environment. I am grateful for the interesting talks during lunch breaks, for valuable insights on the IceCube Collaboration and your continuous advice and support.

Finally, I wish to thank my parents for fully supporting me throughout my studies here in Münster and my sister for helping me find the last little mistakes in my thesis. Thank you for everything!

Declaration of Academic Integrity

I hereby confirm that this thesis, entitled "Measurement of the optical properties of PMT components and investigation of their influence on the simulated PMT response" is solely my own work and that I have used no sources or aids other than the ones stated. All passages in my thesis for which other sources, including electronic media, have been used, be it direct quotes or content references, have been acknowledged as such and the sources cited. I am aware that plagiarism is considered an act of deception which can result in sanction in accordance with the examination regulations.

Signature:		Timos	Sand	
Date:	17.09	0.2025		

I consent to having my thesis cross-checked with other texts to identify possible similarities and to having it stored in a database for this purpose.

I confirm that I have not submitted the following thesis in part or whole as an examination paper before.

Signatı	ire: Timos	Sand	
Date:	17.09.2025		